Circulation Research

ORIGINAL RESEARCH

Extracellular Kir2.1^{C122Y} Mutant Upsets Kir2.1-PIP_2 Bonds and Is Arrhythmogenic in Andersen-Tawil Syndrome

Francisco M. Cruz, Álvaro Macías, Ana I. Moreno-Manuel, Lilian K. Gutiérrez, María Linarejos Vera-Pedrosa, Isabel Martínez-Carrascoso, Patricia Sánchez Pérez, Juan Manuel Ruiz Robles, Francisco J. Bermúdez-Jiménez, Aitor Díaz-Agustín, Fernando Martínez de Benito, Salvador Arias-Santiago, Aitana Braza-Boils, Mercedes Martín-Martínez, Marta Gutierrez-Rodríguez, Juan A. Bernal, Esther Zorio, Juan Jiménez-Jaimez, José Jalife

BACKGROUND: Andersen-Tawil syndrome type 1 is a rare heritable disease caused by mutations in the gene coding the strong inwardly rectifying K^+ channel Kir2.1. The extracellular Cys (cysteine)$_{122}$-to-Cys$_{154}$ disulfide bond in the channel structure is crucial for proper folding but has not been associated with correct channel function at the membrane. We evaluated whether a human mutation at the Cys$_{122}$-to-Cys$_{154}$ disulfide bridge leads to Kir2.1 channel dysfunction and arrhythmias by reorganizing the overall Kir2.1 channel structure and destabilizing its open state.

METHODS: We identified a Kir2.1 loss-of-function mutation (c.366 A>T; p.Cys122Tyr) in an ATS1 family. To investigate its pathophysiological implications, we generated an AAV9-mediated cardiac-specific mouse model expressing the Kir2.1^{C122Y} variant. We employed a multidisciplinary approach, integrating patch clamping and intracardiac stimulation, molecular biology techniques, molecular dynamics, and bioluminescence resonance energy transfer experiments.

RESULTS: Kir2.1^{C122Y} mice recapitulated the ECG features of ATS1 independently of sex, including corrected QT prolongation, conduction defects, and increased arrhythmia susceptibility. Isolated Kir2.1^{C122Y} cardiomyocytes showed significantly reduced inwardly rectifier K+ (I_{K1}) and inward Na+ (I_{Na}) current densities independently of normal trafficking. Molecular dynamics predicted that the C122Y mutation provoked a conformational change over the 2000-ns simulation, characterized by a greater loss of hydrogen bonds between Kir2.1 and phosphatidylinositol 4,5-bisphosphate than wild type (WT). Therefore, the phosphatidylinositol 4,5-bisphosphate–binding pocket was destabilized, resulting in a lower conductance state compared with WT. Accordingly, on inside-out patch clamping, the C122Y mutation significantly blunted Kir2.1 sensitivity to increasing phosphatidylinositol 4,5-bisphosphate concentrations. In addition, the Kir2.1^{C122Y} mutation resulted in channelosome degradation, demonstrating temporal instability of both Kir2.1 and $Na_V1.5$ proteins.

CONCLUSIONS: The extracellular Cys$_{122}$-to-Cys$_{154}$ disulfide bond in the tridimensional Kir2.1 channel structure is essential for the channel function. We demonstrate that breaking disulfide bonds in the extracellular domain disrupts phosphatidylinositol 4,5-bisphosphate–dependent regulation, leading to channel dysfunction and defects in Kir2.1 energetic stability. The mutation also alters functional expression of the $Na_V1.5$ channel and ultimately leads to conduction disturbances and life-threatening arrhythmia characteristic of Andersen-Tawil syndrome type 1.

GRAPHIC ABSTRACT: A graphic abstract is available for this article.

Key Words: andersen syndrome ■ arrhythmias, cardiac ■ death, sudden, cardiac ■ membrane potentials ■ organisms, genetically modified ■ tachycardia, ventricular ■ ventricular fibrillation

In This Issue, see p 951 | Meet the First Author, see p 952

Correspondence to: Francisco Miguel Cruz, PhD, Cardiac Arrhythmia Laboratory, Centro Nacional de Investigaciones Cardiovasculares, Melchor Fernández Almagro 3, 28029 Madrid, Spain, Email fmcruz@cnic.es; or José Jalife, MD, PhD, Cardiac Arrhythmia Laboratory, Centro Nacional de Investigaciones Cardiovasculares, Melchor Fernández Almagro 3, 28029 Madrid, Spain, Email jjalife@cnic.es

Supplemental Material is available at https://www.ahajournals.org/doi/suppl/10.1161/CIRCRESAHA.123.323895.
For Sources of Funding and Disclosures, see page e69.

Circulation Research is available at www.ahajournals.org/journal/res

Novelty and Significance

What Is Known?

- Andersen-Tawil syndrome type 1 is a rare inheritable arrhythmogenic disease caused by loss-of-function mutations in *KCNJ2*, the gene encoding the strong inward rectifier potassium channel Kir2.1 responsible for I_{K1}.
- Extracellular Cys (cysteine)$_{122}$ and Cys_{154} form an intramolecular disulfide bond that is essential for proper Kir2.1 channel folding but not considered vital for channel function.
- Replacement of Cys_{122} or Cys_{154} residues in the Kir2.1 channel with either alanine or serine abolished ionic current in *Xenopus laevis* oocytes.

What New Information Does This Article Contribute?

- A single residue mutation causing a break in the extracellular Cys_{122}-to-Cys_{154} disulfide bond leads to Kir2.1 channel dysfunction and arrhythmias in part by reorganizing the overall Kir2.1 channel structure, disrupting phosphatidylinositol 4,5-bisphosphate–dependent Kir2.1 channel function, and destabilizing the open state of the channel.
- Defects in Kir2.1 energetic stability alter the functional expression of the voltage-gated cardiac sodium channel $Na_V1.5$, one of the main Kir2.1 interactors in the macromolecular channelosome complex, contributing to the arrhythmias.
- The data support the idea that susceptibility to arrhythmias and sudden cardiac death in Andersen-Tawil syndrome type 1 are specific to the type and location of the mutation so that clinical management should be different for each patient.

Altogether, our research illuminates the mechanisms of arrhythmias and sudden cardiac death in Andersen-Tawil syndrome type 1. The results underscore the dual function of the extracellular Cys122-to-Cys154 disulfide bond in the Kir2.1 channel in both maintaining interaction with phosphatidylinositol 4,5-bisphosphate and energetically stabilizing the Kir2.1-$Na_V1.5$ channelosome complex. Disruption of that function by the $Kir2.1^{C122Y}$ mutation ultimately leads to arrhythmias in Andersen-Tawil syndrome type 1. The results may lead to the identification of new molecular targets in the future design of drugs to treat a human disease that currently has no defined therapy.

Nonstandard Abbreviations and Acronyms

AAV	adeno-associated virus
AP	action potential
ATS1	Andersen-Tawil syndrome type 1
BRET	bioluminescence resonance energy transfer
cTnT	cardiac troponin T
Cys	cysteine
MD	molecular dynamic
Nluc	nanoluciferase
PIP_2	phosphatidylinositol 4,5-bisphosphate
PVT	polymorphic ventricular tachycardia
RMP	resting membrane potential
RyR2	ryanodine receptor
SERCA	Ca2+-ATPase
SR	sarcoplasmic reticulum
TMD	transmembrane domain

Andersen-Tawil syndrome type 1 (ATS1) is a rare, inheritable autosomal dominant disease caused by loss-of-function mutations in the *KCNJ2* gene, which codes the strong inward rectifier potassium channel Kir2.1.[1,2] Kir2.1 is ubiquitously expressed throughout the human body, and ATS1 mutations predispose patients to a triad of alterations including periodic paralysis, dysmorphias, and arrhythmias that can lead to sudden cardiac death[3,4] by mechanisms that remain unclear.[5] In the heart, Kir2.1 is responsible for the inward rectifier K^+ current (I_{K1}),[6] which plays a central role in the maintenance of the resting membrane potential (RMP) and the final phase of action potential (AP) repolarization.[7] Therefore, loss-of-function mutations in Kir2.1 lead to a substantial decrease in I_{K1}, with consequent membrane depolarization at rest, as well as AP duration and corrected QT (QTc) interval prolongation.[8] Normal Kir2.1 channel function requires agonist phosphatidylinositol 4,5-bisphosphate (PIP_2) interactions, which stabilizes the G-loop in the open state. Defects in PIP_2 binding are a major pathophysiologic mechanism underlying the loss-of-function phenotype for several ATS1-associated mutations.[5,9–11]

The primary structure of the human Kir2.1 channel comprises a total of 13 Cys (cysteine) residues distributed along each monomer. Cys residues are uniquely reactive providing the ability to form disulfide bonds.[12] They contribute to the structural stability of proteins while being key target sites for redox-related processes.[13] Thus, Cys mutations may affect the tridimensional structure of the channel and alter its function. Seven Cys are expected to be distributed in the Kir2.1 channel N- and C-terminus regions, but mutation in most of them has not been

shown to significantly affect the single-channel conductance nor the channel open probability.[14] However, mutating Cys_{76} and Cys_{311} to polar or charged residues modulated the interaction between Kir2.1 and PIP_2 and resulted in either an absence of channel activity or a decrease in open probability.[14] Similarly, class Ic antiarrhythmic drugs have been shown to bind to the Cys_{311} residue of the Kir2.1 channel and to reduce the polyamine-induced inward rectification increasing the outward I_{K1}.[15,16] Four Cys residues are located in the channel transmembrane segment TM1 (Cys_{89} and Cys_{101}), the pore (Cys_{149}), and TM2 regions (Cys_{169}). Importantly, the remaining 2 Cys, Cys_{122} and Cys_{154}, are located at extracellular space positions absolutely conserved across the inward rectifier family[17] and forming a disulfide bond crucial for channel assembly.[12,18,19] However, the Cys_{122}-to-Cys_{154} disulfide bridge has not been considered essential for normal Kir2.1 function once the channel has been formed.[12]

Here, we report on an ATS1 family with a novel Kir2.1 loss-of-function mutation in Cys_{122} (c.366 A>T; p.Cys122Tyr; C122Y) with a high prevalence of ventricular arrhythmias, which, in the case of the proband, required implantation of an intracardiac defibrillator. To study the molecular mechanisms underlying life-threatening arrhythmias produced by the $Kir2.1^{C122Y}$ mutation, we have generated a mouse model of ATS1 using adeno-associated virus (AAV) $Kir2.1^{C122Y}$ gene transfer that recapitulates the ATS1 phenotype. We used a multidisciplinary approach that included patch clamping and intracardiac electrophysiological stimulation, molecular biology, molecular dynamic (MD) modeling, and bioluminescence resonance energy transfer (BRET). We demonstrate that a disulfide bond break in the Kir2.1 extracellular domain disrupts PIP_2-dependent regulation, leading to channel dysfunction and defects in Kir2.1 energetic stability. The mutation also alters the functional expression of $Na_V1.5$ and ultimately leads to life-threatening arrhythmias that characterize ATS1.

METHODS

Data Availability

The authors declare that all supporting data are available within the article. Please see the Major Resources Table and Supplemental Methods for more details.

Ethics Statement

All animal experiment procedures conformed to EU Directive 2010/63EU and Recommendation 2007/526/EC. We obtained skin biopsies from one patient carrying the $Kir2.1^{C122Y}$ mutation after written informed consent, and consent to publish, in accordance with the Ethical Committee for Research of Centro Nacional de Investigaciones Cardiovasculares and the Carlos III Institute (CEI PI58_2019-v3), Madrid, Spain. The local ethics committees and the Animal Protection Area of the Comunidad Autónoma de Madrid (PROEX 111.4/20) approved the animal protocols.

Mice

We obtained 4- to 5-week-old C57BL/6J mice of both sexes from the Charles River Laboratories. The animals were reared and housed in accordance with the Centro Nacional de Investigaciones Cardiovasculares animal facility guidelines and regulations.

Adeno-Associated Virus Vector Production, Purification, and Mouse Model Generation

We generated AAV vectors using the cardiomyocyte-specific cTnT (cardiac troponin T) proximal promoter and encoding a human version (CCDS11688.1) of wild-type Kir2.1 ($Kir2.1^{WT}$) or the ATS1 Kir2.1 mutant ($Kir2.1^{C122Y}$), followed by tdTomato report. Vectors were packaged into AAV serotype 9 and produced by the triple-transfection method, using HEK293T cells as described previously.[20,21] Mice were anesthetized with ketamine (60 mg/kg) and xylazine (20 mg/kg) via the intraperitoneal route. Thereafter, 3.5×10^{10} virus particles were inoculated intravenously through the femoral vein in a final volume of 50 µL. Only well-inoculated animals were included in the studies. All experiments were performed 8 to 10 weeks after infection. Ex vivo fluorescent signal confirming cardiac expression and distribution of protein expression was assessed as described.[22]

Echocardiography

Transthoracic echocardiography was performed blindly by an expert operator using a high-frequency ultrasound system (Vevo 2100, VisualSonics, Inc, Canada) with a 40-MHz linear probe and analyzed as described in the Supplemental Methods.

Surface ECG Recording

Mice were anesthetized using isoflurane inhalation (0.8%–1.0% volume in oxygen) and maintained at 37 °C in a heating plate. Four-lead surface ECGs were recorded for 5 minutes using subcutaneous limb electrodes connected to an MP36R amplifier unit (BIOPAC Systems). Data acquisition and analysis were performed using the AcqKnowledge software.

In Vivo Intracardiac Recording and Stimulation

An octopolar catheter (Science) was inserted through the jugular vein and advanced into the right atrium and right ventricle as previously described.[23] Atrial and ventricular arrhythmia inducibility was assessed by applying consecutive trains at 10 and 25 Hz, respectively.

Cardiomyocyte Isolation

The procedure was performed as described by Macías et al[24] (Supplemental Methods).

Membrane Fractionation, Immunoprecipitation, and Immunoblotting

The total protein was obtained from both isolated ventricular $Kir2.1^{WT}$ and $Kir2.1^{C122Y}$ cardiomyocytes using RIPA buffer (150-mmol/L NaCl, 10-mmol/L Tris-HCl, 1-mmol/L ethylenediaminetetraacetic acid, 1% Triton X-100, 0.1% sodium dodecyl sulfate [SDS], and 0.1% sodium deoxycholate) supplemented with protease inhibitor cocktail (Roche, 11836170001) and Pierce BCA Protein Assay Kit (Thermo Fisher). A total amount of 50 µg of protein was resolved in each lane on 10% SDS-PAGE gels, electrotransferred onto a 0.2-µm PVDF membrane

(BioRad, 1704150), and probed with specific antibodies. For membrane fractionation, cells were extracted and homogenized in an ice-cold homogenization medium. After lysis, the protein extract was processed according to the manufacturer's specifications (Abcam, ab65400). Please see further details in the Major Resources Table and Supplemental Methods.

BRET Lipid–Binding Assay

HEK293T cells were transfected with 2 µg of plasmid encoding Kir2.1^{WT} or Kir2.1^{C122Y} protein fused with Nluc (nanoluciferase) in the C-terminal region. After 48 hours, the BRET assay was done in a 96-well plate as previously described.[25] See the Supplemental Methods for details.

Patch Clamping in Isolated Cardiomyocytes

Electrophysiological studies were performed in isolated cardiomyocytes from both ventricles. The whole-cell patch-clamp technique, data analysis procedures, and internal and external solutions (Table S1) were similar to those previously described.[9–13] Details are presented in the Supplemental Methods.

Calcium Dynamics Assays

Cytosolic Ca^{2+} was monitored according to previously described protocols.[26–28] Briefly, cells were loaded with Fluo-4-AM (Invitrogen). Fluorescence was detected in line scan mode (usually 2 ms/scan), with the line drawn approximately through the center of the cell and parallel to its long axis.

Dynamic Modeling to Predict Kir2.1-PIP$_2$ Interaction

For each monomer, we used the preopened state of Kir2.2 bound to PiP$_2$ as a template (Protein Data Bank code 3SPH) to conduct MD modeling. We generated homology PiP$_2$ models binding to Kir2.1^{WT}, Kir2.1^{C122Y} homotetramer, and Kir2.1$^{WT/C122Y}$ heterotetramer to study Kir2.1-PiP$_2$ interactions using 2000-ns MD. The CHARMM-GUI (a well-recognized versatil program for atomic-level simulation and molecular modeling) server allowed us to simulate both the membrane and the environment. Please see Supplemental Methods for a detailed description of the procedures.

Statistical Analyses

To determine the statistical power and minimum sample size in our experiments, we did a power calculation using R base power.t.test or power.anova.test function depending on the data analysis. We used a significance level (α=0.05), power (1−β=80%) and the estimated difference between control and experimental data for *t* test and estimated variances for ANOVA. We used GraphPad Prism software, versions 7.0 and 8.0. For non-Gaussian distributions, we applied the nonparametric Mann-Whitney *U* test. We used 1- or 2-way ANOVA corrected by the Šídák multiple comparisons test. We used the Grubb test for outliers. To determine whether the spatial distribution of the Grp1-associated scaffold protein 65 signal obeys any organizational rule, the observed patterns were compared using de F-function as previously described.[29] No across-test multiple-test correction was applied (ie, only within-test corrections were made). Data are expressed as mean±SEM, and differences are considered significant at $P<0.05$ (*$P<0.05$; **$P<0.01$; ***$P<0.001$; and ****$P<0.0001$). Note that N refers to the number of mice used and n refers to the number of cells analyzed per mouse or transfection. All precise *P* values are presented in statistical analysis data in the Supplemental Material.

RESULTS

Life-Threatening Arrhythmias in an ATS1 Family With the Kir2.1^{C122Y} Mutation

We screened a family with members suffering numerous idiopathic sudden loss-of-consciousness episodes using a targeted sequencing gene panel involved in arrhythmias (*RYR2*, *CASQ2*, *TRDN*, *CALM1*, and *KCNJ2*). We identified a novel de novo potential pathogenic heterozygous missense variant c.365 A>T; p.Cys122Trp of the *KCNJ2* gene for ATS1 (LQTS type 7) in 2 family members (Figure 1A and 1B; Table S2). The proband (patient II.2) was a 16-year-old female of White origin who experienced several sudden loss of consciousness events of unknown origin. Initially, patient II.2 was diagnosed with mitral valve prolapse of the anterior leaflet without hemodynamic repercussions. The electrophysiological study was negative following hospital admission for syncope and subsequent evidence of polymorphic ventricular extrasystoles refractory to antiarrhythmic drugs (propafenone, mexiletine, and lidocaine). She continued with propranolol treatment (120 mg/d) combined with oral mexiletine (200 mg/8 hours). At the age of 23 years, a single-chamber intracardiac defibrillator was implanted after several episodes of syncopal polymorphic ventricular tachycardia (PVT) and registering 3 appropriate discharges throughout the age of 25 to 35 years during sodium channel blocker administration (Figure 1C). ECG analysis revealed a corrected QT interval in the upper limit of the normal range (470 ms) with pronounced U waves and polymorphic extrasystoles with frequent trigeminy episodes (Figure 1D). She is now 45 years old and currently under treatment with 120-mg/d nadolol and 25-mg/d spironolactone. The proband's son (patient III.1) remains asymptomatic at the age of 8 years. However, ECG analysis revealed a prolonged QTc interval of 490 ms with a widened T wave and prominent U waves (Figure 1E), consistent with ATS1 symptoms.

Cardiac Conduction Defects and Arrhythmias in Kir2.1^{C122Y} Mice

The AAV approach allowed us to evaluate the disease-causing Kir2.1^{C122Y} mutation without the need for tedious, costly, and time-consuming backcrosses, significantly reducing the use of animals in research (3R's principle). The gene therapy approach using AAVs has been used successfully to generate various arrhythmogenic disease models, such as Brugada syndrome,[30] catecholaminergic polymorphic ventricular tachycardia,[31] and ATS1.[24] We used intravenous AAV–mediated cardiac-specific gene transfer[22] to generate male and female mice expressing human Kir2.1^{WT} or Kir2.1^{C122Y} proteins. We confirmed AAV infection throughout the heart with cardiomyocytes stably expressing the specific targeted transgenes (Figure S1). Our analysis corresponded to a cardiomyocyte transduction rate

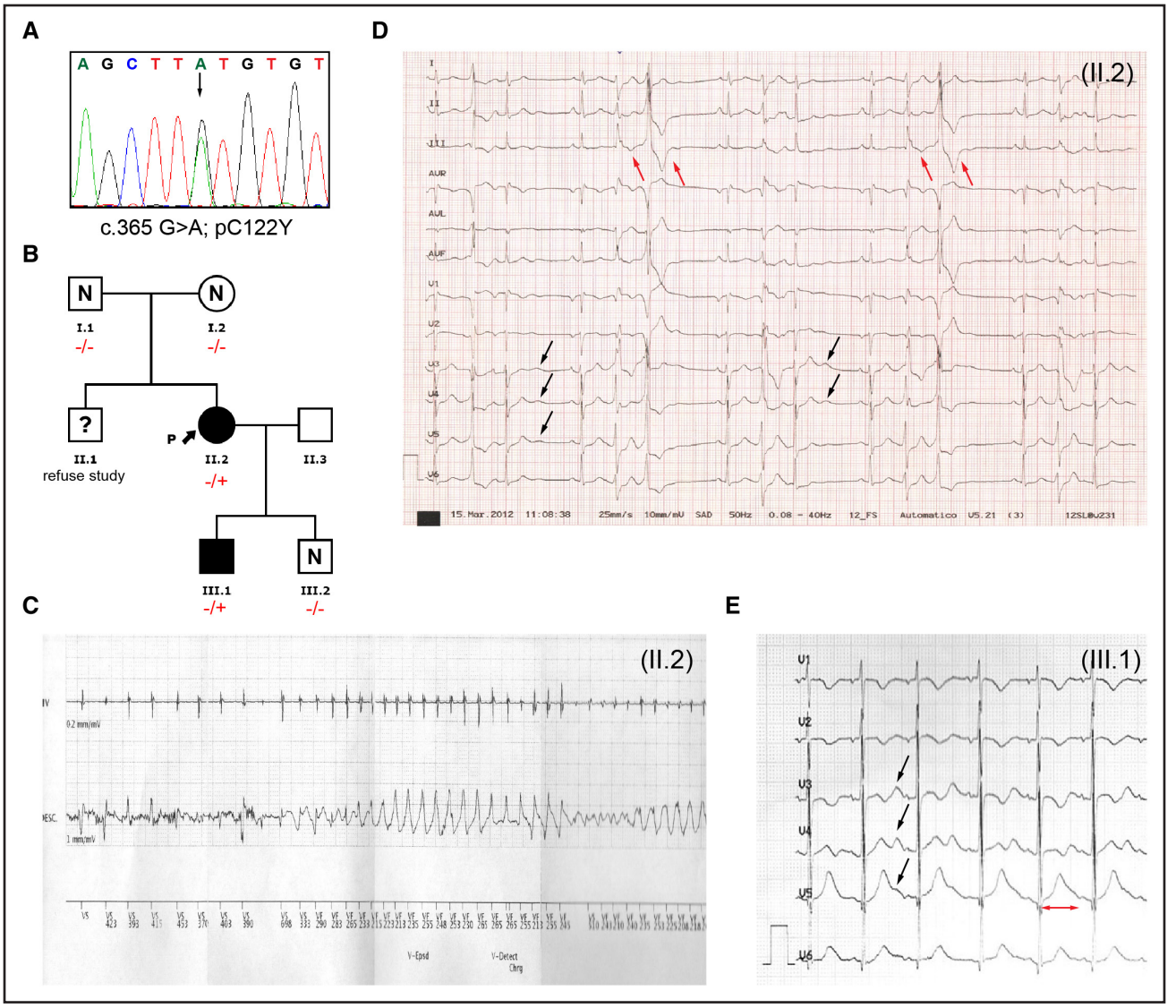

Figure 1. Genetics and ECG phenotype of Andersen-Tawil syndrome type 1 family members with Kir2.1^{C122Y} mutation.
A, DNA sequences derived from proband's genomic DNA. The trace shows a heterozygous substitution of guanine to adenine resulting in the C122Y amino acid change. **B**, Family pedigree according to the carrier status of the p.Cys122Tyr *KCNJ2* gene variant. Squares and circles indicate males and females, respectively. Mutation carriers are (–/+) and noncarriers are ($^{-/-}$). Uncertain mutation carriers are (?) and nonaffected are (N). Phenotype-positive individuals are in black. The black arrow points to proband (P). **C**, Twelve-lead ECG of proband (II.2) at the age of 23 years, showing an episode of syncopal polymorphic ventricular tachycardia during sodium channel blocker (mexiletine; 600 mg/day) treatment combined with β-blocker therapy (propranolol; 20 mg/12 h). **D**, ECG of the proband (II.2) showing typical Andersen-Tawil syndrome abnormalities. Black arrows point to prominent U waves. Red arrows point to bidirectional ventricular extrasystoles. **E**, ECG from individual III.1 demonstrating genotype-phenotype segregation. Black arrows point to prominent U waves. The red line highlights a broad T wave and prolonged corrected QT interval (510 ms).

(quantified by Tdtomato immunofluorescence) of around 95% (Figure S1C). Analysis by k-means clustering for segmented images showed that cell fluorescence intensities clustered around integer values, with >60% of cardiomyocytes having a signal intensity that corresponded to a viral genome number between 1 and 3 (Figure S1C). These data confirm that AAV infection occurs throughout the heart and that cardiomyocytes stably express the specific targeted Kir2.1 transgene. Total protein analysis demonstrated that isolated Kir2.1^{WT} and Kir2.1^{C122Y} cardiomyocytes have similar Kir2.1 protein levels compared with untransfected mice (Figure S1D and S1E). In addition, quantitative real-time polymerase chain reaction (qRT-PCR) showed that, like the untransfected group, Kir2.1^{WT} and Kir2.1^{C122Y} mouse hearts amplified, at similar levels, the endogenous mouse mRNA of the *KCNJ2* gene, indicating that our AAV-models did not operate in a haploinsufficiency scenario (Figure S1F). Moreover, evaluation of heart weigh-to-body weight ratio and echocardiography showed no cardiac morphology changes or contractile dysfunction, respectively, in AAV-transduced mice (Figure S2). On surface ECG, Kir2.1^{C122Y} mice showed conduction alterations characteristic of the disease in male and female AAV-transduced mice (Figure 2A). More importantly, Kir2.1^{C122Y} mice had frequent

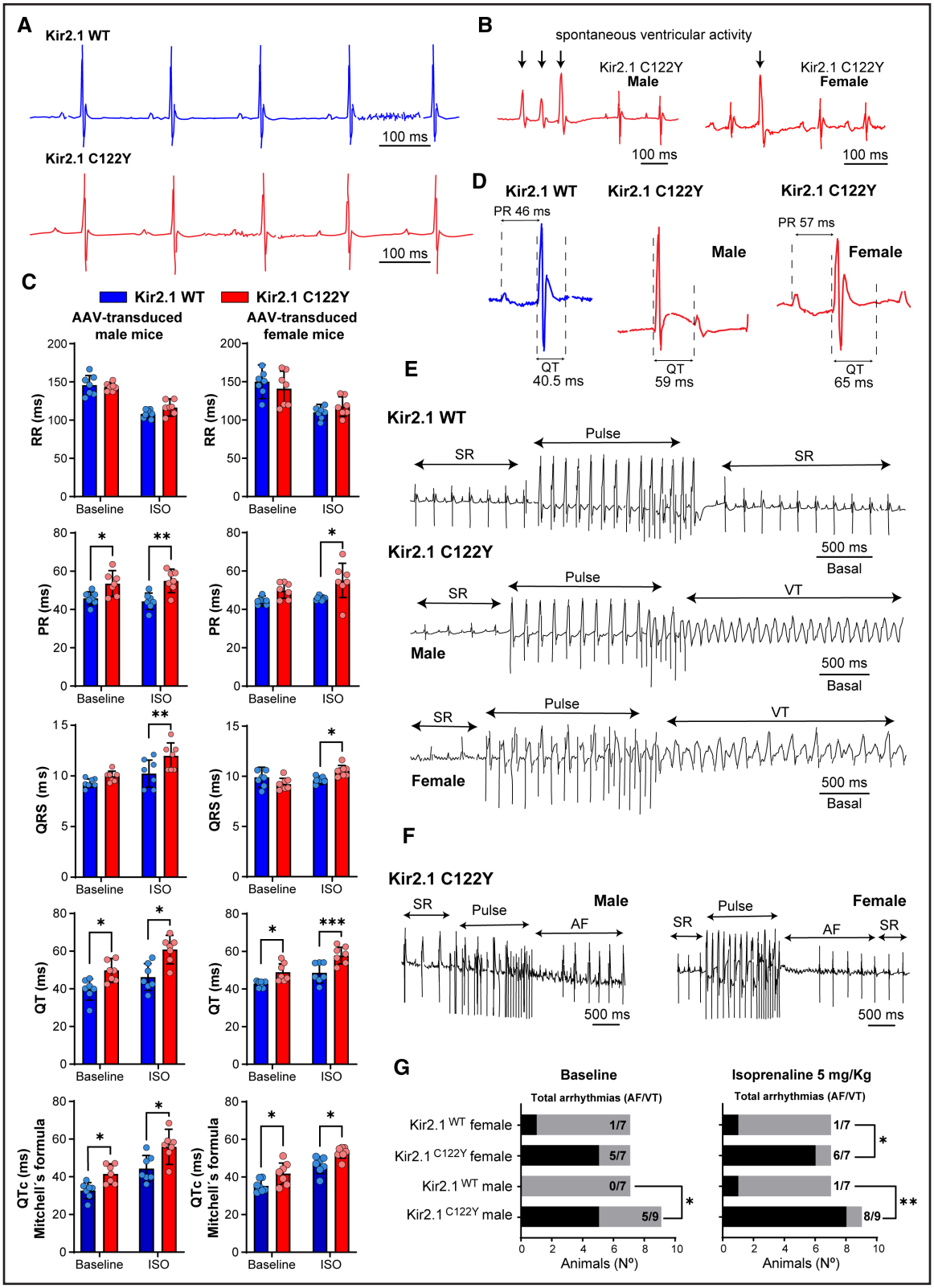

Figure 2. Kir2.1^{C122Y} mice recapitulate the Andersen-Tawil syndrome type 1 patients' phenotype and increased sex-independent susceptibility to arrhythmias.

A, Representative lead-II ECG recordings from adeno-associated virus (AAV)–transduced Kir2.1^{WT} (**top**) and Kir2.1^{C122Y} (**bottom**) mice. The record shows normal sinus rhythm with prolonged PR and corrected QT (QTc) interval in mutant animals (N=7 animals per group). **B**, ECG in a Kir2.1^{C122Y} male and female animals showing frequent premature ventricular complexes manifested as duplets. **C** and **D**, Effects of isoproterenol (ISO, 5 mg/Kg) administration on electrical conduction, and QT and QTc (Mitchell correction) intervals in Kir2.1^{C122Y} male and female animals compared with baseline condition. Each value is the mean±SEM (N=7 animals per group; 2-way ANOVA corrected by the Šídák multiple (*Continued*)

premature ventricular complexes and runs of nonsustained PVT (Figure 2B) in agreement with the ATS1 patient's phenotype. Under stress conditions induced by isoproterenol (5 mg/Kg), Kir2.1^{C122Y} mice developed PR and QRS prolongation. Compared with control, Kir2.1^{C122Y} animals exhibited repolarization abnormalities with prolongation of the QTc interval and occasional overlap of the T wave with the P wave of the following complex (Figure 2C and 2D). Intracardiac stimulation of the right atrium or right ventricle used consecutive trains of stimuli at 10 and 25 Hz. Under baseline conditions, Kir2.1^{C122Y} mice had a significantly increased arrhythmia susceptibility with respect to Kir2.1^{WT} (Figure 2E and 2F); on stimulation, 5 of 9 (55.5%) and 5 of 7 (71.4%) Kir2.1^{C122Y} male and female mice, respectively, developed atrial or ventricular arrhythmias, including PVT, compared with 0 of 7 and 1 of 7 Kir2.1^{WT} male and female mice (0%–14.2%). Isoproterenol administration increased arrhythmia susceptibility in both atria and ventricles of Kir2.1^{C122Y} (8 of 9 male mice, 88.9%; 6 of 7 female mice, 85.7%), versus Kir2.1^{WT} (1 of 7 male and female mice, 14.2%). Altogether, these results indicate that the Kir2.1^{C122Y} mutation recapitulates the ATS1 patient's cardiac electrical phenotype, establishing a sex-independent arrhythmogenic substrate.

Kir2.1^{C122Y} Subunits Are Able to Form Heterotetramers

Kir2.1 channels can exist either as homotetrameric or heterotetrameric complexes consisting of either 4 identical Kir2.1 subunits or in various combinations with the structurally related members of the Kir2.x subfamily of inward rectifier K^+ channels.[32] To clarify the mechanisms by which the C122Y mutation causes channel dysfunction in ATS1, we determined whether Kir2.1^{C122Y} can assemble with wild type (WT) subunits and traffic to the surface membrane (Figure S3). Immunoprecipitation studies using differently tagged Kir2.1 subunits were used to assess whether the mutation affected subunit assembly. The HA and Myc epitope tags were incorporated into an external site that does not perturb channel activity[33,34] (Figure S3A). In these studies, HEK293T cells were either cotransfected with Myc-tagged Kir2.1 (WT) or HA-tagged Kir2.1 (WT or C122Y) at a 1:1 ratio. Recovered immunoprecipitants on anti-HA-bound beads were resolved by SDS-PAGE, and the extent of HA-tagged channel subunit interaction was assessed using anti-Myc antibodies in immunoblots. As shown by the representative experiment (Figure S3B), the wild-type Myc-Kir2.1 coimmunoprecipitated with both HA-tagged subunits, indicating that the mutation does not alter subunit interaction. In addition, immunocytochemical analysis of cotransfected cells revealed that the Myc-tagged Kir2.1^{WT} and HA-tagged Kir2.1^{C122Y} subunits are highly colocalized (Figure S3C), offering further evidence that the C122Y subunits are capable of assembling with the WT subunits in cells.

Kir2.1^{C122Y} Subunits Traffic to the Cardiomyocyte Surface Membrane

Kir2.1 localizes at 2 separate well-defined striated microdomains running parallel to each other at ≈0.9-μm intervals throughout the cardiomyocyte.[24] One microdomain corresponds to the t-tubules where Kir2.1 colocalizes with the voltage-gated cardiac sodium channel $Na_V1.5$ (≈1.8-μm spacing). The other is at the sarcoplasmic reticulum (SR) where Kir2.1 functions to control calcium homeostasis (Figure 3A and 3B).[24] Disruption of 1 or both microdomains leads to malfunction of Kir2.1 and $Na_V1.5$ channels that might trigger arrhythmias. However, unlike the defective distribution pattern that was demonstrated for the trafficking deficient mutation Kir2.1$^{\Delta 314\text{-}315}$,[24] immunolocalization and confocal image analysis of isolated ventricular cardiomyocytes from Kir2.1^{C122Y} animals revealed an unaltered distribution pattern for both Kir2.1 and $Na_V1.5$ channels (Figure 3A and 3B). When we determined the percentage of membrane expression using an anti-Na^+/K^+ ATPase immunostaining, the results again showed a similar distribution of Kir2.1 and $Na_V1.5$ channels in Kir2.1^{WT} and Kir2.1^{C122Y} cells, with a small but significant reduction in $Na_V1.5$ accumulation level in mutant cardiomyocytes (Figure 3C). Similarly, on the western blot, the Kir2.1 protein level was alike in untransfected and AAV-transduced mice (Figure 3D). However, the $Na_V1.5$ protein level was lower for the mutant cardiomyocytes in sarcolemmal-enriched fraction and in total protein (Figure 3E; Figure S4). Trafficking of both Kir2.1 and $Na_V1.5$ to their membrane microdomains depends in part on their classical route that involves incorporation into clathrin-coated vesicles at the trans-Golgi network marked by interaction with the adaptor protein complex-1 ϒ-adaptin subunit (AP-1).[35] Trafficking may also occur via an unconventional route directly from SR in a GRASP (Grp1-associated scaffold protein)-dependent manner.[36] To test whether Kir2.1^{C122Y} disrupts Kir2.1 trafficking, we analyzed AP-1

Figure 2 Continued. comparisons test). *P<0.05. **P<0.01. ***P<0.001. **E**, Representative lead-II ECG traces of Kir2.1^{WT} (**top**) and Kir2.1^{C122Y} male (**middle**) and female (**bottom**) mice before (sinus rhythm [SR]), during and after intracardiac application of stimulus trains at 10 and 25 Hz under baseline conditions. Ventricular stimulation in a Kir2.1^{C122Y} mouse induced polymorphic ventricular tachycardia (VT). **F**, Representative lead-II ECG traces after atrial stimulation in Kir2.1^{C122Y} male (**left**) and female (**right**) mice. Atrial stimulation induced an episode of atrial fibrillation (AF). **G**, Contingency plots of the number of animals with the arrhythmogenic response after intracardiac stimulation at baseline and after treatment with ISO (5 mg/Kg). Each value is the mean±SEM (N=7 female and Kir2.1^{WT} male mice and N=9 Kir2.1^{C122Y} male mice; the Fisher exact test (presence/absence arrhythmias). *P<0.05. **P<0.01. WT indicates wild type.

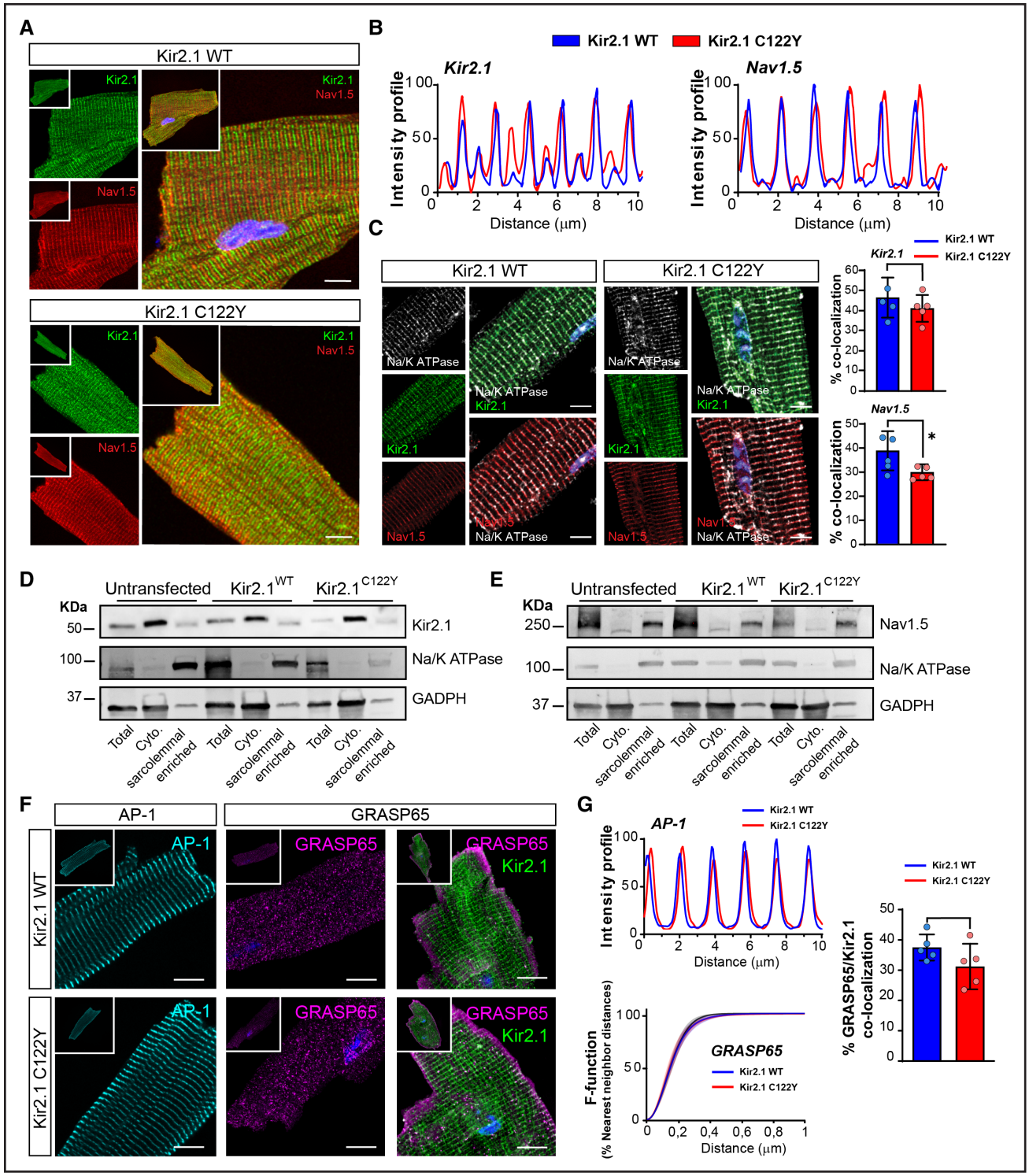

Figure 3. Kir2.1^{C122Y} cardiomyocytes preserve Kir2.1 and Na$_V$1.5 protein trafficking, but both proteins are reduced at the sarcolemma. **A**, Representatives confocal images of Kir2.1 and Na$_V$1.5 channels in Kir2.1^{WT} and Kir2.1^{C122Y} cardiomyocytes. Scale bar, 10 μm. **B**, Fluorescence intensity profiles show distribution patterns for both Kir2.1 (**left**) and Na$_V$1.5 (**right**) channels in Kir2.1^{WT} and Kir2.1^{C122Y} cardiomyocytes. Note double banding for Kir2.1 indicating sarcoplasmic reticulum (SR) expression. **C**, Representative immunofluorescence images show colocalization of Kir2.1 (green) and Na$_V$1.5 (red) with Na/K ATPase (white) at the sarcolemma. Scale bar, 10 μm. Graphs show the percentage of colocalization with significantly reduced Na$_V$1.5. Each value is the mean±SEM (N=5 animals per group; n=10 [WT] and n=12 [C122Y] cells; nonparametric Mann-Whitney *U* test; *P<0.05). **D** and **E**, Western blots comparing cytosolic and sarcolemmal Kir2.1 and Na$_V$1.5 in Kir2.1^{WT} vs Kir2.1^{C122Y} cardiomyocytes. **F**, Representatives confocal images of classical action potential (AP)-1 and unconventional (GRASP65; Grp1-associated scaffold protein 65) trafficking routes for Kir2.1 and Na$_V$1.5. Scale bar, 10 μm. **G**, Quantification of fluorescence intensity profiles for AP-1, F-function (% nearest neighbor distances), and percentage of GRASP (Grp1-associated scaffold protein) colocalization in isolated Kir2.1^{WT} and Kir2.1^{C122Y} cardiomyocytes. Each value is the mean±SEM (N=5 animals per group; n=7 [WT] and n=9 [C122Y] cells; nonparametric Mann-Whitney *U* test). WT indicates wild type.

and Grp1-associated scaffold protein 65 by immunofluorescence of both WT and mutant cardiomyocytes. As shown in Figure 3F and 3G, the AP-1 expression profile was identical in both groups. Similarly, Grp1-associated scaffold protein 65 staining presented an F-function distribution (distance from particles to nearest neighbor particle) with no statistically significant differences between WT or mutant groups. Also, colocalization of Kir2.1 with Grp1-associated scaffold protein 65 was similar in both groups. From the foregoing, the Kir2.1^{C122Y} variant is able to form heterotetramers with WT subunits and retains trafficking ability. Taken together, these observations strongly suggest that the C122Y mutation leads to cardiac electrical alterations via mechanisms other than those recently demonstrated for the trafficking deficient Δ314-315 mutation.[36] This led us to further explore the biophysical and electrophysiological properties of the Kir2.1^{C122Y} channel and determine whether the mutation directly alters potassium conductance and disrupts protein stability.

Kir2.1^{C122Y} Cardiomyocytes Exhibit Defects in Excitability and Action Potential Duration

We performed patch-clamping experiments in isolated cardiomyocytes from Kir2.1^{WT} and Kir2.1^{C122Y} expressing hearts. We focused on both I_{K1} and the sodium inward current (I_{Na}) to evaluate whether the impulse conduction disturbances and arrhythmias observed in this model of ATS1 are due to defects in 1 or both currents. The results show a 90% reduction in the outward I_{K1} density of Kir2.1^{C122Y} compared with Kir2.1^{WT}cardiomyocytes (Figure 4A; Figure S5A). Furthermore, surprisingly, Kir2.1^{C122Y} cardiomyocytes showed a slight but significant decrease in I_{Na} density compared with controls (Figure 4B; Figure S5B) with significant changes in the voltage-dependence of current activation properties of $Na_V1.5$ but similar time-dependent kinetics at −40 mV (Figure S6). These data further demonstrate that while the mutant Kir2.1 protein traffics and is expressed at the membrane, it is dysfunctional and also reduces the $Na_V1.5$ function. Thus, these results reinforce the hypothesis that conduction disturbances and arrhythmias in patients with ATS1 are due to a defect in cardiomyocyte excitability.

As illustrated in Figure 4C through 4E, current-clamp recordings revealed that while Kir2.1^{WT} cardiomyocytes had stable RMPs with a mean value of −70.03±1.61 mV, most isolated Kir2.1^{C122Y} cardiomyocytes were substantially depolarized, unable to respond to external stimulation. As shown in Figure 4D, of 11 successfully patched Kir2.1^{C122Y} cardiomyocytes, 4 (36.36%) were continuously oscillating, whereas 7 (63.63%) showed bistability with some generating rapidly discharging slow responses. In addition, they were either continuously oscillating from a maximum diastolic potential of −28.5±3.5 mV or alternating spontaneously between 2 distinct levels of membrane potential (MP_{1-2}) with mean values of −44.9 and −22 mV (Figure 4E). Because the membrane potential oscillations and spontaneous discharges were likely calcium channel-mediated, we analyzed the intracellular calcium dynamics in both WT and ATS1 mice. Confocal images of Ca^{2+} dynamics showed that Kir2.1^{C122Y} cardiomyocytes had multiple abnormal spontaneous calcium release events during systole and diastole, with patterns similar to those observed in the AP bistability (Figure 4F). Because Ca^{2+} movements across the SR are controlled by the RyR2 (ryanodine receptor)-mediated Ca^{2+} release and the SERCA (Ca^{2+}-ATPase)-mediated Ca^{2+} reuptake to-and-from the cytosol and SR lumen, we wondered whether protein alteration could happen in the Kir2.1^{C122Y} mouse model. Immunolocalization and confocal image analysis of isolated ventricular cardiomyocytes revealed similar costaining percentages of Kir2.1^{WT} and Kir2.1^{C122Y} with both RyR2 and SERCA proteins (Figure 4G and 4H; Figure S7). In addition, protein expression was also similar (Figure 4I). Because K^+ flux across Kir2.1 SR channels contributes countercurrent to Ca^{2+} movement,[24] we analyzed the intracellular Ca^{2+} dynamics in both controls and ATS1 mice (Figure 4J). Cardiomyocytes expressing Kir2.1^{WT} and Kir2.1^{C122Y} showed similar Ca^{2+} transient decay under acute caffeine administration in intact cardiomyocytes (Figure 4J). These results indicate that the Ca^{2+} alterations are due to functional defects at the sarcolemma, including RMP depolarization and reduced excitability, rather than Kir2.1 dysfunction at the SR.

Ex Vivo Optical Mapping Shows Defective Cardiac Conduction Velocity and Reentrant Arrhythmias in Kir2.1^{C122Y} Mouse Hearts

We conducted optical mapping experiments to probe the pathophysiological significance of I_{K1} and I_{Na} reduction in isolated Kir2.1^{C122Y} cardiomyocytes. We used the voltage-sensitive fluorescent dye FluoVolt in Langendorff-perfused hearts paced at different frequencies. Color phase mapping revealed that maximum conduction velocity was significantly slower in Kir2.1^{C122Y} hearts (≈31.8 cms^{-1}) compared with Kir2.1^{WT} (≈51.9 cms^{-1}; Figure 5A and 5B). The restitution curve showed significantly slower conduction velocities in Kir2.1^{C122Y} hearts at all frequencies tested (Figure 5B). In addition, Kir2.1^{C122Y} hearts were also more inducible for sustained and nonsustained reentrant arrhythmias of variable duration (0 of 5, 0% in Kir2.1^{WT} versus 3 of 5, 60% in Kir2.1^{C122Y}; Figure 5C and 5D). Optical pseudo-ECG and AP recordings showed distinct types of complex arrhythmic events. The slow upstroke velocities likely reflect the reduced I_{Na} magnitude. These data provide proof that by decreasing cell excitability in isolated cardiomyocytes, Kir2.1^{C122Y} also reduces conduction velocity leading to reentry and PVT.

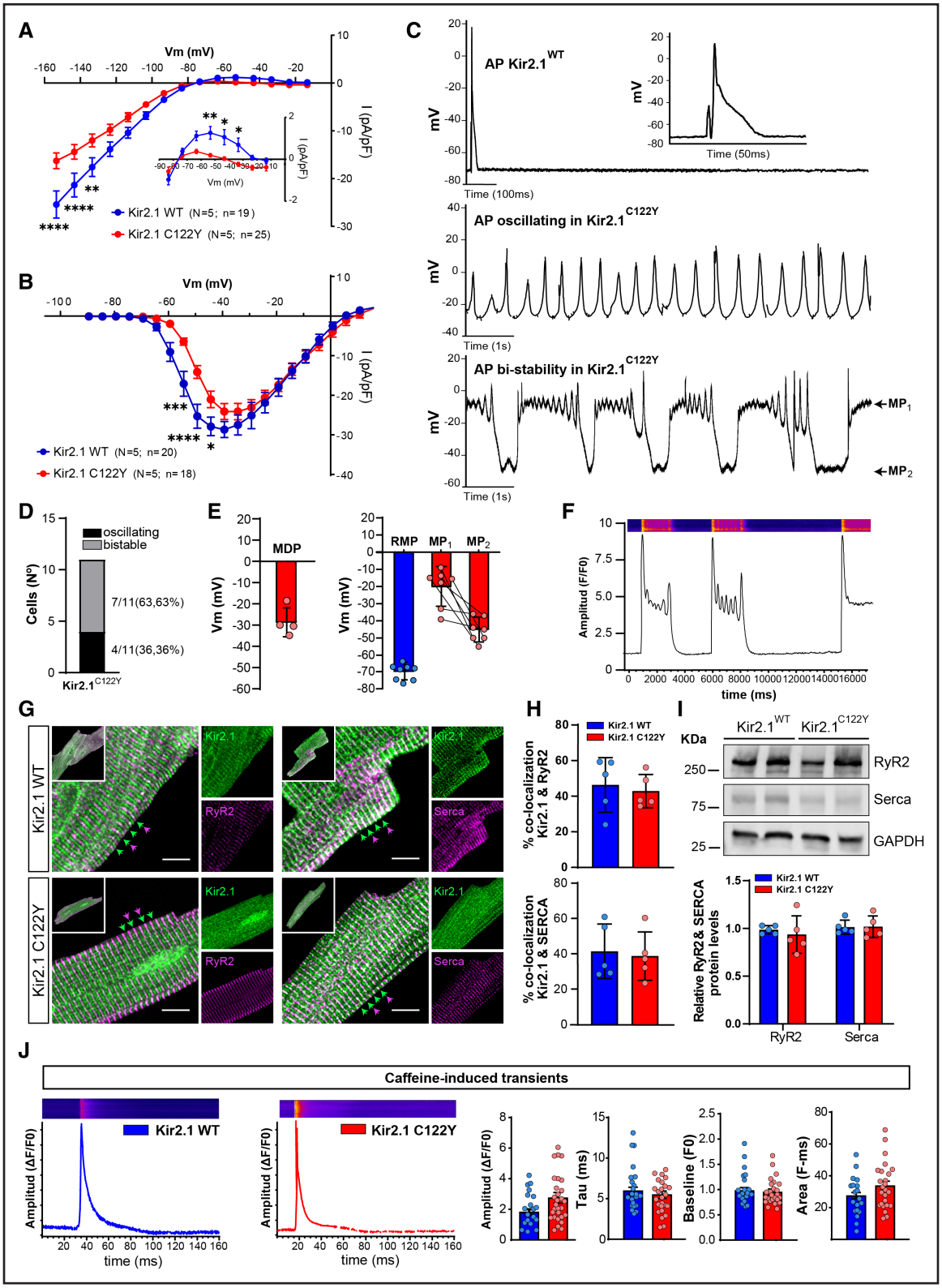

Figure 4. Kir2.1^{C122Y} alters isolated mouse cardiomyocyte electrophysiology.

A, Superimposed I_{K1} current-voltage (IV) relationships for Kir2.1^{WT} (blue; N=5, n=19) and Kir2.1^{C122Y} (red; N=5, n=25) cardiomyocytes. **B**, Superimposed I_{Na} IV relationships for Kir2.1^{WT} (blue; N=5, n=20) and Kir2.1^{C122Y} (red; N=5, n=18) cardiomyocytes. Each value is the mean±SEM (2-way ANOVA corrected by the Šídák multiple comparisons test (*P<0.05; **P<0.01; ***P<0.001; and ****P<0.0001). **C**, Current-clamp recordings of isolated Kir2.1^{WT} (**top**, adjusted inset of action potential [AP]) and Kir2.1^{C122Y} cardiomyocytes showing oscillating (**middle**) and 2 distinct levels of resting membrane potential (RMP) with spontaneous bursting (bistability, **bottom**). **D**, Quantification of cell number in oscillating or bistable state. **E**, Maximum diastolic potential (MDP) of spontaneously active Kir2.1^{C122Y} cardiomyocytes (**right**), RMP of Kir2.1^{WT} (blue), (*Continued*)

Disulfide Bond Loss Reorganizes Tridimensional Channel Structure Interfering With Kir2.1^{C122Y}-PIP_2 Binding

Cys_{122} localizes at the extracellular loop of the Kir2.1 channel, immediately after the first transmembrane domain (TMD), where it is cross-linked by an intramolecular disulfide bond with Cys_{154} at the beginning of the second transmembrane α-helix (Figure 6A). Both residues and their disulfide bond are conserved across the Kir family (Figure 6B), which is crucial for proper channel folding, as they may help accommodate the extracellular loop in an optimal tridimensional structure.[18] Notably, we found that the Cys_{122}-to-Cys_{154} disulfide bond is also highly conserved among all analyzed species, including humans and mice (Figure 6C). We used in silico homology modeling to derive predictions of the molecular structure of the Kir2.1^{C122Y} mutant channel and, thus, understand the possible mechanisms underlying its dysfunction. Atomic-level modeling showed that compared with the WT channel, Kir2.1^{C122Y} undergoes a clear reorganization (TMscore, 0.73 and RDMS, ≈6 Å for homotetramer or TMscore, 0.78 and RDMS, ≈7 Å for heterotetramer; Figure 6D and 6E). The Gibbs free-energy values for Kir2.1^{C122Y} were more positive compared with WT (WT, 4801.404 versus C122Y, −4131.754 for homotetramer and −2274.207 for heterotetramer; Figure 6E). This indicates a more unstable state in Kir2.1^{C122Y} homotetrameric and heterotetrameric channels, suggesting that the incorporation of mutant subunit could affect the integrity of the WT monomers or even affect the macromolecular channelosome complex, including Kir2.1 and $Na_V1.5$.

To predict Kir2.1-PIP_2 interaction ability, we incorporated PIP_2 molecules in the simulation. Our results showed an altered Kir2.1^{C122Y}-PIP_2 interaction following a dominant-negative pattern. The Kir2.1$^{WT/C122Y}$ heterotetramer presented 2 of 4 PIP_2 molecules compared with the complete set of 4 PIP_2 in the Kir2.1^{WT} homotetramer, 1 per monomer (Figure 6F). Notably, the Kir2.1^{C122Y} homotetramer abolished completely PIP_2 interaction, in accordance with the I_{K1} current suppression in homozygous mutant conditions in C154F[37] and C122Y-expressing HEK293T cells (Figure S8). Taken together, these in silico homology experiments predict that the loss of the highly conserved extracellular Cys_{122}-to-Cys_{154} disulfide bond in channels containing the Kir2.1^{C122Y} isoform may result in a clear atomic restructuration with loss of function by mechanisms that include, at least in part, a pronounced interference with the PIP_2-binding pocket.

Cys_{122}-Cys_{154} Disulfide Bond Breakup Disrupts Kir2.1-PiP_2 Interaction

We conducted in silico MD studies to more rigorously establish whether the extracellular Cys_{122}-to-Cys_{154} disulfide bond breakup in the Kir2.1^{C122Y} mutant channel disrupts Kir2.1-PIP_2 interaction (Figure 7). We generated Kir2.1 homology models bound to a single PIP_2 molecule per monomer in Kir2.1^{WT}, Kir2.1^{C122Y} homotetramer, and Kir2.1$^{WT/C122Y}$ heterotetramer to study Kir2.1-PIP_2 interactions throughout a 2000-ns MD simulation (see the Supplemental Methods for details of the overall approach). For each monomer, we used the preopened state of Kir2.2 bound to PIP_2 as a template (Protein Data Bank code 3SPH).[38] The CHARMM-GUI server allowed us to simulate both membrane and environment (Figure 7A and 7B); we then performed 3 independent replicas for each model. First, we evaluated the conformational changes in the extracellular space by monitoring either the C_{122} or Y_{122} backbone dihedral angles along the 2000-ns MD. Analysis showed only 28% conserved frames in backbone dihedral angles, while 72% presented a shift in Φ-dihedral angle from around −70° to −140° shortly after the first 100 ns (Figure 7C; Figure S9). The Y_{122} sidechain reorientation resulted in the movement of D_{112} and the consequent break of the internal hydrogen-bonding network between D_{112} and the H_{110} sidechain and the NH backbone of C_{122} within the extracellular loop (Figure S10). Thus, hydrogen bonds between the H_{110} sidechain and the Y_{122} backbone were either absent or generally present in <50% of the frames. In addition, in several MD simulations, a new hydrogen bond was formed between D_{112} and K_{117}. Therefore, C122Y leads to a reorganization of the hydrogen-bonding network of the extracellular loop that might alter the Kir2.1 function (Table S3). Nevertheless, neither of the 2 Y_{122} conformations observed in the MD led to a significant change in the relative disposition of the outer and inner helices, as shown by the measurement of the distance between 2 opposite residues (I_{106} and I_{156}) located near the extracellular side of each of those helices (Figure S11).

Figure 4 Continued. and 2 distinct levels of membrane potential (MP_{1-2}) of bistable Kir2.1^{C122Y} cardiomyocytes (red; **right**). Each value is the mean±SEM. **F**, Representative confocal image and profile of calcium transient dynamics in a representative Kir2.1^{C122Y} cardiomyocyte. Note bistability amplitude and large numbers of spontaneous calcium release events spreading throughout the cell. **G**, Representative immunolocalization images of RyR2 (ryanodine receptor) and SERCA (Ca^{2+}-ATPase) in adeno-associated virus (AAV)–transduced ventricular cardiomyocytes from Kir2.1^{WT} and Kir2.1^{C122Y} mice. Scale bar, 10 µm. **H**, Quantification of the percentage of colocalization between Serca2a and RyR2 proteins with Kir2.1 in AAV-transduced hearts. Each value is the mean±SEM (N=5 animals per group; n=15 (WT) and n=18 (C122Y) cells; nonparametric Mann-Whitney *U* test). **I**, Western blots showing similar amounts of total protein for both (N=5 animals per group; 2-way ANOVA corrected by the Šídák multiple comparisons test). **J**, Representative fluorescence profiles of caffeine-induced calcium release in Kir2.1^{WT} and Kir2.1^{C122Y} cardiomyocytes. Graphs show amplitude (ΔF[F-F0]/F0), tau (decay kinetics), and baseline of each caffeine-induced Ca^{2+} transient, as well as the total area. Each value is the mean±SEM (N=5 animals per group; n=19 [WT] and n=25 [C122Y] cells; nonparametric Mann-Whitney *U* test). WT indicates wild type.

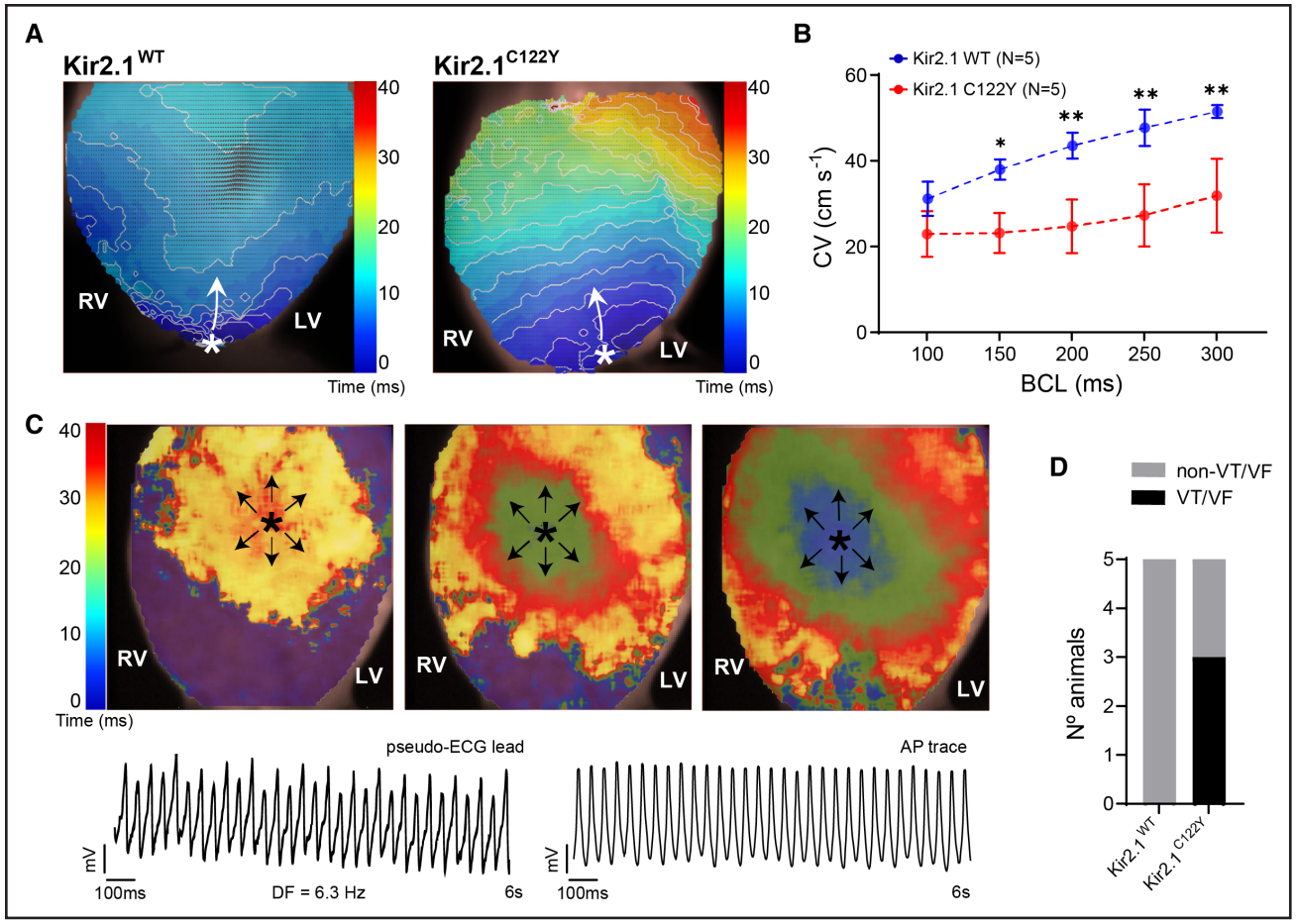

Figure 5. Cardiac conduction defects and reentrant arrhythmias in Kir2.1^{C122Y} mouse hearts.
A, Representative single camera pixel recording from an optical mapping experiment shows velocity maps with 1-ms activation isochrones in Kir2.1^{WT} (**left**) and Kir2.1^{C122Y} (**right**) hearts paced at BCL of 300 ms. The color bar indicates conduction velocity (CV; cms^{-1}). The white asterisk indicates the pacing point; the propagation direction is indicated by the curved white arrow. **B**, CV restitution curve displayed slower velocities in Kir2.1^{C122Y} heart at all frequencies tested. Both groups presented slightly slower velocities at higher frequencies. Each value is the mean±SEM (N=5 per condition; 2-way ANOVA corrected by the Šídák multiple comparisons test; *P<0.05; **P<0.01). **C**, Phase mapping of polymorphic ventricular tachycardia (VT) in Kir2.1C122Y hearts. The bottom figures show pseudo-ECG lead (**left**) and single-pixel optical action potential (AP) trace (**right**) during VT maintained by 1 self-sustaining rotor of 6.3 Hz of frequency. The reentry center (singularity point) during VT is indicated by a black asterisk, and black arrows indicate the direction. **D**, Contingency plots of the number of hearts show arrhythmia inducibility for each group. Data show a high rate of arrhythmia susceptibility in Kir2.1^{C122Y} hearts. Each value is the mean±SEM (N=5 animals per group; the Fisher exact test for contingency data). BCL, basic cycle length; DF indicates domint frequency; LV, left ventricle; RV, right ventricle; VF, ventricular fibrillation; and WT, wild type.

Kir2.1-PIP$_2$ interactions involve hydrophobic contacts with PIP$_2$ acyl chains and more specific polar interactions between PIP$_2$ phosphates and positively charged Kir2.1 residues at the TMD-to-cytoplasmic domain interface.[38,39] A detailed study of the atomic Kir2.1-PIP$_2$ hydrogen-bonding distance yielded a global loss of hydrogen bonds in the Kir2.1^{C122Y} channels that directly affected PIP$_2$ interactions. Comprehensive analysis of the $R_{80}W_{81}R_{82}$ motif and the lysine-cluster $K_{182}K_{185}K_{187}K_{188}$ of the helicoidal cytoplasmic domain-to-TMD linker (C-linker; Figure 7D) showed a clear reduction in hydrogen-bonding capacity in both heterotetrameric and homotetrameric Kir2.1^{C122Y} channels throughout the 2000-ns MD (Figure 7F; Table S4). Our simulations predict that compared with the Kir2.1^{WT} tetramers, Kir2.1$^{WT/C122Y}$ and Kir2.1^{C122Y} channels lose, at a higher rate, the characteristic hydrogen bond of the PIP$_2$ 1′ phosphate with $R_{80}W_{81}R_{82}$, particularly R_{82}, and the PIP$_2$ 4′ and 5′ phosphates with the C-linker (Table S4). As expected, the unmutated chains (chains A and C) in Kir2.1$^{WT/C122Y}$ heterotetramers showed similar behavior to WT chains (Table S4).

On PIP$_2$ binding at the interface between TMD and cytoplasmic domain, the C-linker undergoes a disorder-to-order transition bringing both domains closer together. Thus, the G-loop wedges into the TMD causing the inner helix gate to open.[38] Follow-up of this transition showed that the C-linker loses the hydrogen bonds characteristic of α-helix structures in the Kir2.1^{WT}, Kir2.1^{C122Y} heterotetramer and homotetramer, with only those between K_{188}-E_{191} and R_{189}-T_{192} being preserved along the MD, indicating that N- and C-terminals of the C-linker helix were destructured (Figure 7E; Table S5). Interestingly, at

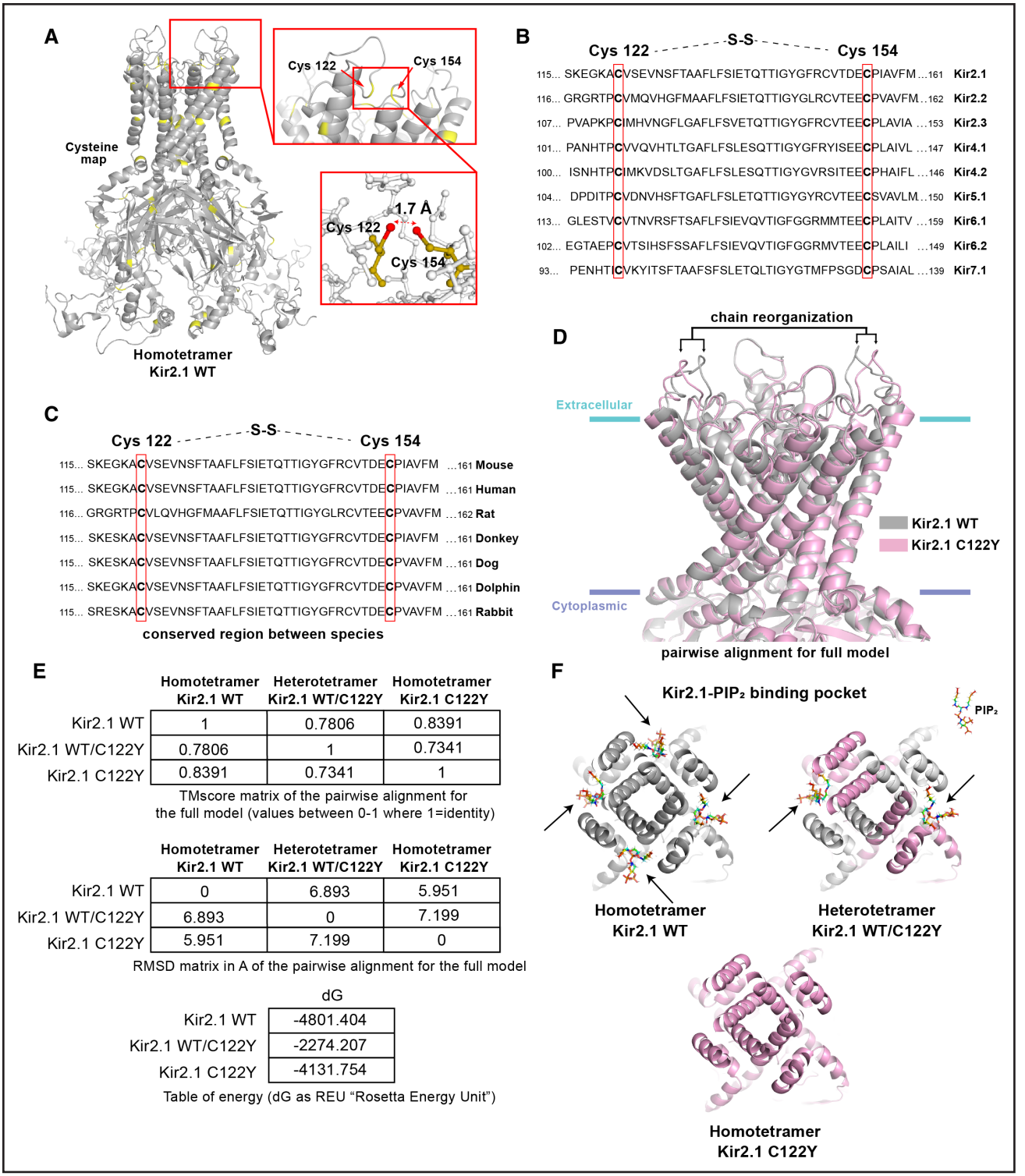

	Homotetramer Kir2.1 WT	Heterotetramer Kir2.1 WT/C122Y	Homotetramer Kir2.1 C122Y
Kir2.1 WT	1	0.7806	0.8391
Kir2.1 WT/C122Y	0.7806	1	0.7341
Kir2.1 C122Y	0.8391	0.7341	1

TMscore matrix of the pairwise alignment for the full model (values between 0-1 where 1=identity)

	Homotetramer Kir2.1 WT	Heterotetramer Kir2.1 WT/C122Y	Homotetramer Kir2.1 C122Y
Kir2.1 WT	0	6.893	5.951
Kir2.1 WT/C122Y	6.893	0	7.199
Kir2.1 C122Y	5.951	7.199	0

RMSD matrix in A of the pairwise alignment for the full model

	dG
Kir2.1 WT	-4801.404
Kir2.1 WT/C122Y	-2274.207
Kir2.1 C122Y	-4131.754

Table of energy (dG as REU "Rosetta Energy Unit")

Figure 6. The C122Y mutation alters Kir2.1 channel conformation and phosphatidylinositol 4,5-bisphosphate (PIP$_2$) binding. **A**, Topological scheme of Kir2.1 homotetramer channel indicating Cys (cysteine) positions (yellow). **B**, Amino acid sequence in the Kir family showing the highly conserved extracellular disulfide bond. Cys$_{122}$ and Cys$_{154}$ are highlighted. **C**, Amino acid sequence alignment of Kir2.1 protein shows highly conserved extracellular disulfide bond between species **D**, Pairwise alignment for the full model (gray, Kir2.1^{WT}; pink, Kir2.1^{C122Y}). **E**, **Top**, TMscore matrix of the pairwise alignment for the full model. Values between 0 and 1, where 1 is the identity. RMSD matrix (**middle**) in angstroms (Å). **Bottom**, Table of Gibbs free-energy values (dG) of WT and mutant homotetramer and heterotetramer. **F**, Docking modeling of Kir2.1-PiP$_2$ interaction in Kir2.1^{WT}, and homotetramer and heterotetramer of Kir2.1^{C122Y} (see text for a detailed explanation of each figure). WT indicates wild type; and RMSD, root-mean-square deviation.

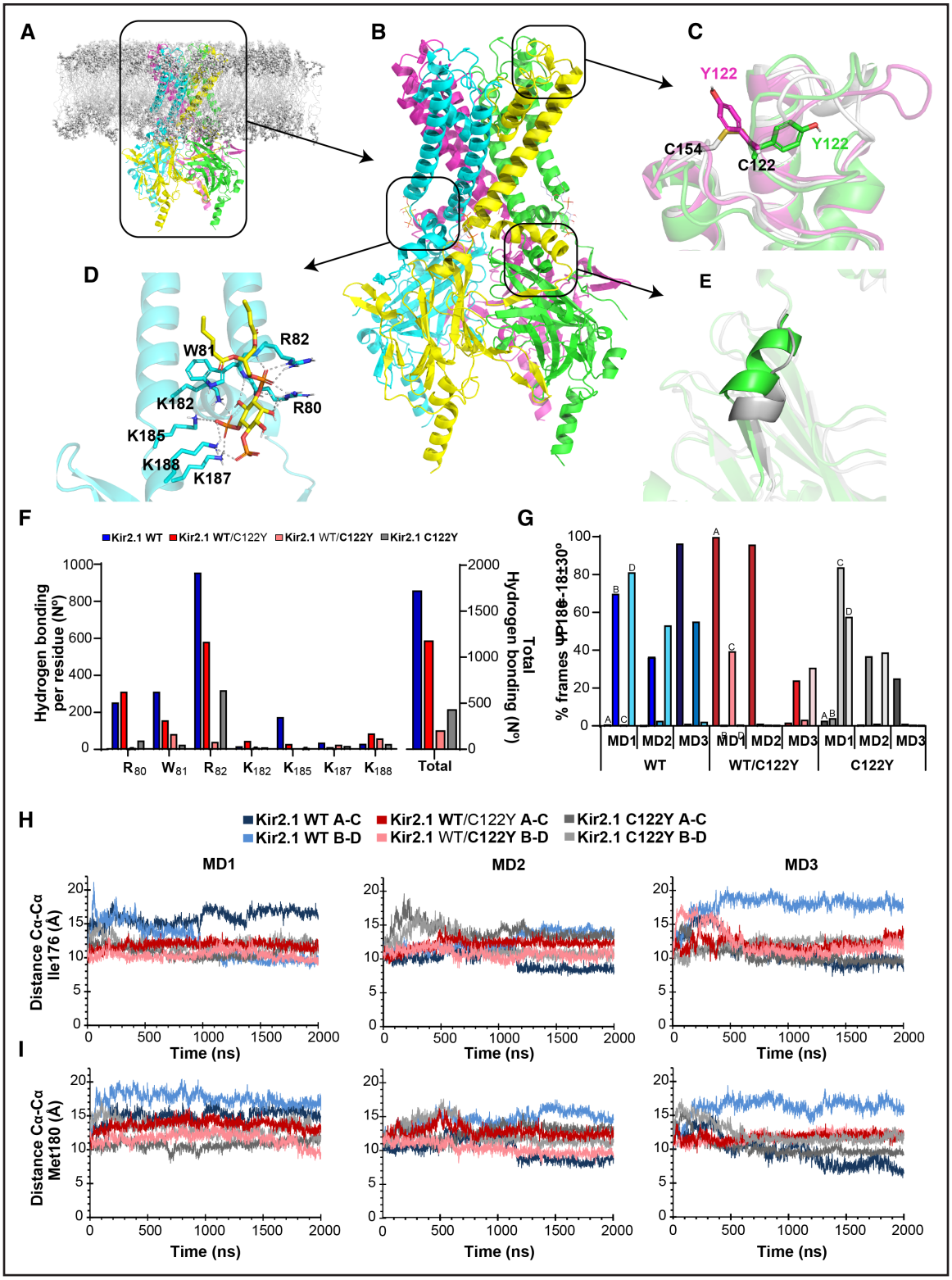

Figure 7. Extracellular disulfide bond break reduces phosphatidylinositol 4,5-bisphosphate (PiP$_2$)–dependent Kir2.1 regulation. **A**, Schematic representation of Kir2.1 tetramer embedded in a bilipid layer. **B**, Structure of Kir tetramer. Monomers are represented in different colors. **C**, Illustrative C122 or Y122 sidechain orientation. Superposition of Kir2.1^{WT} (gray) and 2 representative Kir2.1^{C122Y} monomers (green, the most frequent Y122 orientation; purple, the minor one). **D**, Representative illustration of hydrogen bond network between Kir2.2 and PIP$_2$. The same hydrogen bonds as in the generated homology model were tested for Kir2.1. **E**, Evolution of the C-linker during the molecular dynamic (MD): from a helix (green) to a less structured linker, as shown by a representative 2000-ns snapshot (gray). **F**, Histogram representing the average number of PIP$_2$-Kir2.1 hydrogen bonds per residue along the 2000-ns simulation for Kir2.1^{WT} (blue), Kir2.1$^{WT/C122Y}$ (gray), and Kir2.1$^{WT/C122Y}$ (red). These values are the average of the 3 replicas and the 4 chains for each tetramer. **G**, Histogram representing the (*Continued*)

the beginning of the C-linker motif, the dihedral angles of P_{186} were within those of 3_{10} helix φ (−71) and ψ (−18) in the PIP_2-bound Kir2.1^{WT} structures. However, in the Kir2.1^{C122Y} heterotetramer and homotetramer, the ψ dihedral varied in correlation with a progressive loss of the C-linker's helical character (Figure 7G). Compared with Kir2.1^{WT}, the Kir2.1^{C122Y} homotetramer had a lower percentage of frames with ψ P_{186} dihedral angles within those characteristics of 3_{10} helix structure (Kir2.1^{C122Y}: 17% at 1000 ns and 8% at 2000 ns; Kir2.1^{WT}: 33% at 1000 ns and 17% at 2000 ns), with the percentages of the heterotetramer being intermediate (Figure 7G).

Finally, we measured the distance between Cα carbons of representative pore constriction Ile_{176} and Met_{180} residues at the TM and A_{306} of the G-loop from opposite chains to study the pore opening state during the 2000-ns MD (Figure 7H and 7I; Figure S12).[39,40] For both Ile_{176} and Met_{180}, the distance between the A-B and B-D chains decreased progressively in heterotetrameric and, more pronouncedly, homotetrameric mutant channels, with larger values for WT chains in the first 500 ns, which likely correlated with a more open state in WT channels (Figure 7H and 7I). Longer MD times using WT channels showed that the distance among the Cα carbons of the above residues decreased in 2 opposite monomers and led to an increase in the distance between the other 2 monomers, as observed in the gating mechanism for KirBac3.1.[41] Similarly, the Cα-carbon distance between A_{306} residues in the G-loop slightly decreased in the mutant heterotetramer and, more pronouncedly, homotetramer (Figure S12). These results strongly suggest that the extracellular disulfide bond break in Kir2.1^{C122Y} led to channel closing by altering the Kir2.1-PIP_2 hydrogen-bond network, which, in the WT, stabilizes PIP_2 function to maintain the open state of the channel.

Kir2.1^{C122Y} Has a Reduced Sensitivity To and Binding Capacity for PIP_2

To test for PIP_2 binding to Kir2.1, we fused an Nluc to the C terminus of the channel and used a soluble fluorescent PIP_2 analog suitable for binding to Kir2.1.[25] Activation of Nluc produced a fluorescent PIP_2–dependent BRET signal specific for Kir2.1 as shown by the cartoon of the assay design in Figure 8A. HEK293T cells were transfected with the WT and C122Y mutant versions, respectively, and a bioluminescence assay was performed. We included another Kir2.1 mutant version with a known mutation interfering with PIP_2-Kir2.1 channel interaction as a negative control (Kir2.1^{R218W}). Our results showed that PIP_2 binds with high affinity to Kir2.1^{WT} but, as expected, cannot directly bind to Kir2.1^{C122Y}, such as that we observed for Kir2.1^{R218W} (Figure 8B). To assess the sensitivity of Kir2.1 to PIP_2, we performed inside-out patch clamping of the Kir2.1^{WT} and the heterozygous condition Kir2.1$^{WT/C122Y}$ currents in cotransfected HEK293T cells at a 1:1 ratio. We recorded I_{K1} in both baseline conditions and under increasing concentrations of PIP_2 (25- and 50-μg/ml PIP_2). The results showed that while, in Kir2.1^{WT}, PIP_2 increased the outward K^+ current in a dose-dependent manner, the Kir2.1$^{WT/C122Y}$ mutation blunted the sensitivity to PIP_2. The inward current was unaltered in either group (Figure 8C). As illustrated in Figure 8D, quantification of normalized peak currents (I/I_0) from −30 to +10 mV shows that Kir2.1^{WT}-transfected cells increased progressively with PIP_2, but heterozygous Kir2.1$^{WT/C122Y}$ remained unaltered. Taken together, these results confirm the inability of Kir2.1^{C122Y} channels to functionally interact with PIP_2 molecules that allow proper channel function according to the dominant-negative effect expected from patient data.

DISCUSSION

We report on the first human ATS1 mutation, C122Y, which breaks the Cys_{122}-to-Cys_{154} disulfide bond in the extracellular domain of the tridimensional Kir2.1 structure. We demonstrated that the extracellular Cys_{122}-to-Cys_{154} disulfide bond is essential for the functioning of the Kir2.1 channel, whose disruption leads to defects in PIP_2-dependent regulation, exerting a dominant negative effect with Kir2.1 tetramer channel dysfunction and life-threatening arrhythmias.

Our AAV-mediated mouse model recapitulates in vivo the ECG phenotype of the ATS1 patient carrying the C122Y mutation independently of sex. Isoproterenol administration led to progressive further prolongation in the PR, QRS, and QTc intervals, consistent with the reasonable expectation that AAV affects the electrophysiological properties of contractile cardiomyocytes but also components of the cardiac conduction system. In addition, the mutation increases susceptibility to pacing-induced arrhythmogenic events of high severity (>1 s) in Kir2.1^{C122Y} male and female animals relative to controls, including nonsustained ventricular tachycardias similar to those observed on the proband's ECG. Interestingly, isolated cardiomyocytes from Kir2.1^{C122Y} mice exhibited defects produced by decreased I_{K1} and I_{Na} compared with controls, including a highly depolarized RMP and reduced excitability. They also displayed prolonged AP duration with oscillation and bistability of membrane potential and, in many cases, EADs and spontaneous calcium release events. The bistable RMP shown by some of the Kir2.1^{C122Y} cardiomyocytes may have been, in part,

Figure 7 Continued. percentage of frames in which the ψ dihedral angle of the Pro186 is within those expected for a 3_{10} helix (ψ=−18°±30°). For Kir2.1$^{WT/C122Y}$, (**A**) and (**C**) represent the nonmutated monomers. **H**, I_{176} and **I**, M_{180} Cα-Cα distances between 2 opposite monomers along the 2000-ns MD. Color code on top. N=3 replicates. WT indicates wild type.

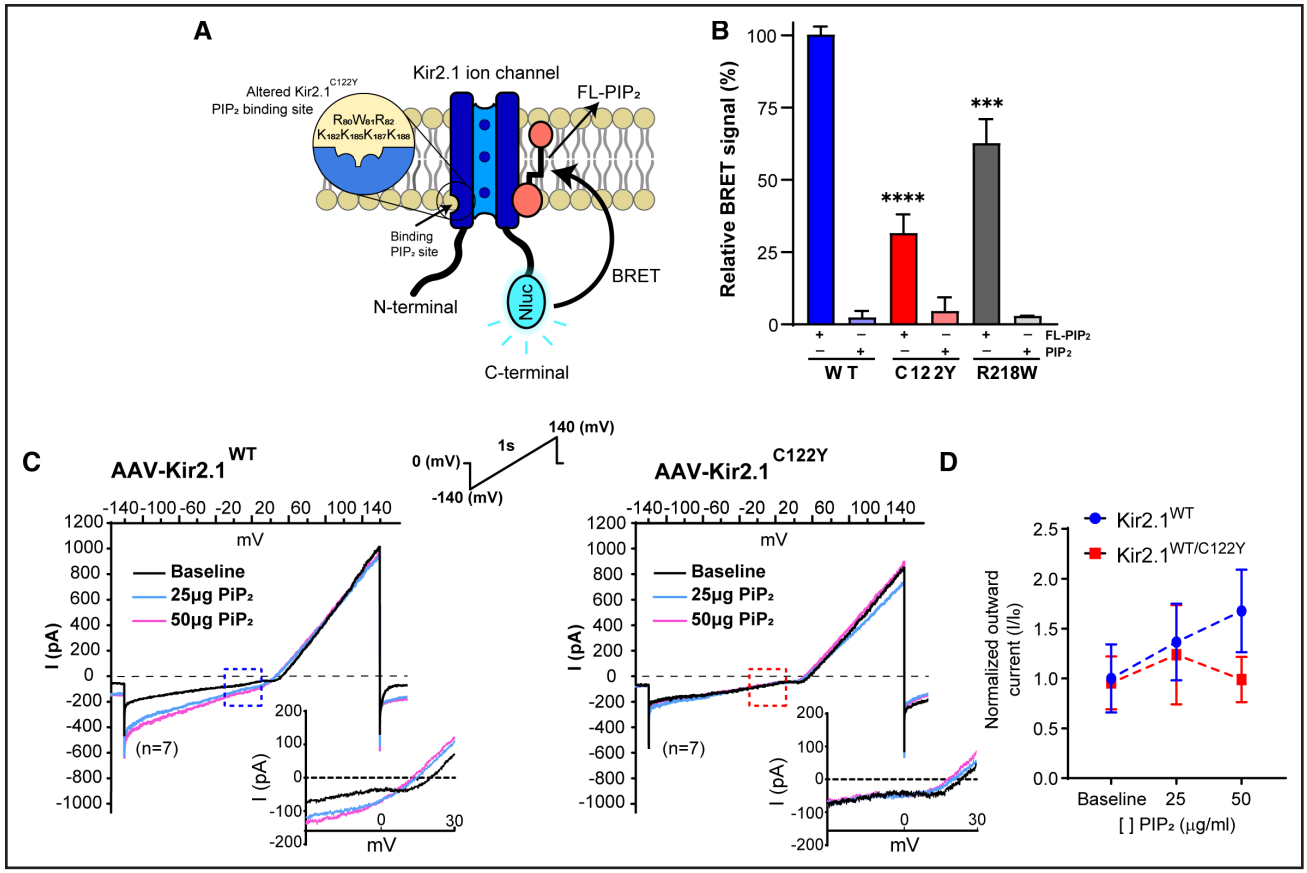

Figure 8. The C122Y mutation reduces Kir2.1-phosphatidylinositol 4,5-bisphosphate (PIP$_2$)–binding capacity and interaction. **A**, Diagram of Kir2.1 monomer fused to the bioluminescent protein Nluc (nanoluciferase; adapted from Cabanos et al[25] with permission). **B**, Specific bioluminescence resonance energy transfer (BRET) signal of binding FI-PIP$_2$ to Kir2.1 WT, C122Y, and R218W and competition with nonfluorescent PIP$_2$ version. C122Y and R218W showed reduced binding. Each value is the mean±SEM (N=3 replicates per group; n=8–10 wells; 2-way ANOVA corrected by the Šídák multiple comparisons test; ****P<0.0001). **C**, Representative inside-out patch recording of I_{K1} in the absence (black current) and the presence of 25 (blue) and 50 (purple) µg/ml of PIP$_2$. The inset shows −30- to 30-mV voltage range. Note that due to the inside-out patch configuration, the recordings seem inverted in both axes compared with the usual whole-cell configuration. **D**, Normalized peak currents (I/I_0) from −30 to +10 mV (dotted boxes); the heterozygous condition abolishes the response to increasing PIP$_2$ concentration. In contrast, in Kir2.1^{WT} cells, outward current increased progressively with the PIP$_2$ concentrations. Both groups maintained an unaltered inward I_{K1} (n=7). Statistical analyses were conducted using 2-way ANOVA corrected by the Šídák multiple comparisons test. AAV indicates adeno-associated virus; and WT, wild type.

due to the modification of the overall I_{K1} current-voltage relation shape produced by the mutation. As demonstrated many years ago by Gadsby and Cranefield[42] in Purkinje fibers, the existence of 2 possible stable resting potentials requires that the net steady-state current-voltage relationship is N-shaped, with 2 zero-current intercepts in regions of positive slope conductance. A third unstable intercept occurs in a region of negative slope conductance. In the case of the Kir2.1^{C122Y} cardiomyocyte, the reduced Kir2.1 outward current at voltages between −60 and 0 mV, counterbalanced by the inward background conductance carried predominantly by sodium and calcium ions, generated an N-shaped current-voltage relation that crossed the voltage axis 3× allowing 2 levels of RMP. Altogether, our results provide a potential mechanism for the spontaneous and induced arrhythmias observed in our ATS1 mouse model.

We included in silico homology modeling and MD to further analyze the structural mechanisms underlying Kir2.1^{C122Y} dysfunction. Interestingly, our results show that loss of extracellular disulfide bond clearly disrupts PIP$_2$-dependent Kir2.1 channel activity despite apparently normal Kir2.1^{C122Y} channel trafficking to the sarcolemma. Kir2.1-PIP$_2$ channel interactions are crucial for channel activity and regulation, and defects in PIP$_2$ binding constitute a major mechanism of Kir2.1 dysfunction underlying the loss of function in several ATS1.[9,43] PIP$_2$ binding is known to induce a large conformational change in Kir channels leading to the formation of 2 new helices, an N-terminal extension of the interfacial helix, and a tether helix at the C-linker.[38,39] The flexible expansion of the C-linker contracts to a compact helical structure involving translation of the cytoplasmic domain ≈6 Å toward the TMD, where it remains anchored and allows the opening of the inner gate of the helix.[38,39,44–46] Our 2000-ns MD simulations with a single PIP$_2$ molecule bound per monomer revealed that the mutation triggered structural changes, particularly the C-linker disorganize faster

in $Kir2.1^{C122Y}$ homotetramer and heterotetramer, which directly modified the PIP_2-binding site.[38] Specifically, the PIP_2 1′ phosphate cap lost its interaction with the $R_{80}W_{81}R_{82}$ triad, particularly R_{82}, which appears strongly bound to WT monomers for longer simulation time (Table S3). These results highlight a rapid release of PIP_2 molecules leading to channel closure, in accordance with the decreases in the Cα-Cα distance observed in the pore constriction residues Ile_{176}, Met_{180}, and A_{306}. In agreement, other studies have shown that P_{186} mutations lead to channel assembly but with significantly reduced PIP_2-binding capacity.[47] Taken together, these results suggest that C122Y induces a reorganization of the chains starting extracellularly and is transmitting along the channel to finally interrupt PIP_2's function. Our experimental results validated the in silico MD predictions and the demonstration by BRET, and inside-out voltage-clamped membrane patches from transfected HEK293T cells showed that the $Kir2.1^{C122Y}$ mutation breaks the disulfide bonds in the Kir2.1 extracellular domain, altering PIP_2-dependent regulation to finally lead to channel dysfunction. Nonetheless, the precise mechanism either by breaking the disulfide bond between Cys_{122}-to-Cys_{154} or the incorporation of a tyrosine residue by which the C122Y mutation interferes with Kir2.1 binding to PIP_2 molecules is beyond the scope of this study and remains to be fully elucidated.

Interestingly, Macías et al[24] have recently shown an SR microdomain of functional Kir2.1 channels contributing to intracellular Ca^{2+} homeostasis that could explain the phenotypic overlapping between ATS1 and catecholaminergic PVT in some patients.[44,45] Ca^{2+} fluxes across the SR membrane are bidirectional and need a charge-compensating countercurrent, ensuring that the SR membrane potential remains near 0 mV during the e-c coupling process.[46,48] Importantly, our results demonstrate that intracellular Ca^{2+} homeostasis was similar in WT and C122Y under acute caffeine administration in intact isolated cardiomyocytes, suggesting that the SR Kir2.1 channel population is not regulated in a PIP_2-dependent manner. However, a role for intracellular Ca^{2+} in arrhythmogenesis provoked by $Kir2.1^{C122Y}$ was evidenced only after overloading the SR by isoproterenol administration. The results suggest that while sarcolemmal $Kir2.1^{C122Y}$ channels fail to conduct potassium through PIP_2-dependent mechanisms, SR $Kir2.1^{C122Y}$ channels remain functional independently of PIP_2 activity. In support of such an idea, Katan et al[49] demonstrated that PiP_2 is exclusively involved in sarcolemmal activities, including controlling Kir2.1 function.

Kir2.1 channels are part of large multiprotein complexes comprising components of the cytoskeleton, regulatory kinases and phosphatases, trafficking proteins, extracellular matrix proteins, and even other ion channels[50–52] This probably explains, in part, the wide variety of clinical phenotypes found in different families with the same mutation and even within the same family.[3] Kir2.1 forms channelosomes with $Na_V1.5$, which indicates that the disease should no longer be considered in the simplistic terms of a monogenic disorder.[2] In fact, as our results show, it would not be correct to assume that the arrhythmic phenotype manifested by the patient is directly due to the mutation in question, but we must also consider potential modifications on the channel's interacting proteins. Therefore, the paradigm-shifting premise of this work is that we can no longer consider inherited arrhythmogenic diseases in terms of dysregulation of a single protein because alteration of any member of a particular multiprotein complex has the potential to modify the function of associated proteins, resulting in a more complex disease. In this sense, the phenotypic manifestations in ATS1 are only understood by considering the wide range of proteins with which the altered ion channels interact.[52] Our results show that $Kir2.1^{C122Y}$ reduces not only I_{K1} but also I_{Na} in isolated mouse cardiomyocytes carrying the mutation. However, the C122Y mutation does not affect the trafficking of either Kir2.1 or $Na_V1.5$ to the sarcolemma, suggesting new regulatory pathways for channelosome function. To further analyze molecular mechanisms involving $Na_V1.5$ regulation, we studied channelosome homeostasis of both Kir2.1 and $Na_V1.5$ proteins due to the differences in Gibbs free-energy values (WT, 4801.404 versus C122Y, −4131.754 for homotetramer or −2274.207 for heterotetramer). Cardiomyocytes were treated with cycloheximide,[53] a ribosomal RNA transcription inhibitor, for periods of 6, 8, 16, 24, and 48 hours at final concentrations of 100 µg/ml (Figure S13). Interruption of protein synthesis resulted in a slight but significant decrease of total Kir2.1 protein after 48 hours of treatment compared with control (Figure S13A). Immunostaining showed a significant increase in Rab5 colocalization, a protein involved in early endosomal formation (Figure S13B), demonstrating temporal instability of the Kir2.1 protein. Similarly, cycloheximide decreased total $Na_V1.5$ protein after 16 hours, which could explain, in part, the reduction in cell surface expression (Figure S13C).

To further confirm Kir2.1-$Na_V1.5$ interaction at the membrane, we silenced scaffolding protein SAP97[54] in neonatal mouse ventricular myocytes. The results show that disruption of the channelosome complex reduced I_{Na} at similar levels in $Kir2.1^{C122Y}$-expressing sh-SAP97 and $Kir2.1^{WT}$/sh-SAP97 cardiomyocytes (Figure S14). These results demonstrate that I_{Na} is affected only when SAP97 mediates the $Na_V1.5$ and $Kir2.1^{C122Y}$ multiprotein complex through PDZ domains.[54–57] Interestingly, a recent study has shown that PIP_2 is a negative regulator of gating properties of NaV1.4 channels,[58] suggesting that it may also be negatively regulating $Na_V1.5$ in our ATS1 mouse model. However, further studies are needed to elucidate the precise mechanisms underlying the impairment of sodium channel activity triggered by $Kir2.1^{C122Y}$, which does not affect channel trafficking. Our data strongly suggest a complex mechanism involved in channelosome dysfunction leading to a slow-conduction substrate for cardiac arrhythmias.

CONCLUSIONS

The potential clinical impact of our results is groundbreaking: understanding the Kir2.1 modulation by its multiple interacting molecules will significantly improve our knowledge of channel function and of inherited and acquired arrhythmogenic cardiac diseases. It should also lay the groundwork for the generation of innovative, effective and safe approaches to prevent sudden cardiac death in these and other devastating cardiac disease. Compared to previous data,[24] all the results shown here support the hypothesis that the molecular mechanisms that increase the susceptibility to arrhythmias and sudden cardiac death in ATS1 are different depending on the specific mutation, so that pharmacological treatment and clinical management should be different for each patient.

ARTICLE INFORMATION

Received October 25, 2023; revision received February 25, 2024; accepted February 29, 2024.

Affiliations

Centro Nacional de Investigaciones Cardiovasculares, Madrid, Spain (F.M.C., A.M., A.I.M.-M., L.K.G., M.L.V.-P., I.M.-C., P.S.P., J.M.R.R., F.J.B.-J., F.M.d.B., J.A.B., J.J.). CIBER (Centro de Investigacion biomédica en Red) de Enfermedades Cardiovasculares, Madrid, Spain (F.M.d.B., J.A.B., E.Z., J.J.). Departments of Medicine and Molecular & Integrative Physiology, University of Michigan, Ann Arbor (J.J.). Servicio de Cardiología (F.J.B.-J., J.J.-J.) and Servicio de Dermatología (S.A.-S.), Hospital Universitario Virgen de las Nieves, Granada, Spain. Instituto de Investigación Biosanitaria de Granada IBS (Instituto de investigaciones biosanitarias), Spain (F.J.B.-J., S.A.-S., J.J.-J.). Unit of Inherited Cardiomyopathies and Sudden Death (CAFAMUSME [Unidad de Cardiopatías Familiares, Muerte Súbita y Mecanismos de Enfermedad]), Health Research Institute La Fe, La Fe Hospital, Valencia, Spain (A.B.-B., E.Z.). Cardiology Department, Hospital Universitario y Politécnico La Fe, Valencia, Spain (A.B.-B., E.Z.). Instituto de Química Médica, Consejo Superior de Investigaciones Científicas, Madrid, Spain (A.D.-A., M.M.-M., M.G.-R.).

Acknowledgments

The authors thank the Centro Nacional de Investigaciones Cardiovasculares (CNIC) Viral Vectors Unit for producing the adeno-associated virus serotype 9. Confocal experiments were conducted at the CNIC Microscopy and Dynamic Imaging Unit. The authors thank the CNIC Bioinformatics Unit for generating the in silico homology modeling simulations, F-function analysis, and helpful discussions. The authors also thank the Centro de Supercomputación de Galicia for the use of the Finis Terrae III supercomputer to perform molecular dynamics studies. The CNIC was supported by the Instituto de Salud Carlos III, the Ministerio de Ciencia, Innovación y Universidades, and the Pro CNIC Foundation and is a Severo Ochoa Center of Excellence (grant CEX2020-001041-S funded by MICIU/AEI/10.13039/501100011033). All authors discussed the results and commented on and approved the article.

Author Contributions

F.M. Cruz and J. Jalife codesigned the experiments. F.M. Cruz performed most of the experiments. A. Macías and A.I. Moreno-Manuel are authors of cellular electrophysiology. F.J.Bermúdez-Jiménez, E. Zorio, and J. Jiménez-Jaimez provided clinical data. L.K. Gutiérrez and F.M. de Benito were in charge of in silico homology modeling and molecular docking studies. A. Díaz-Agustín, M. Martín-Martínez, and M. Gutierrez-Rodríguez performed molecular dynamics simulation and analysis. M. Martín-Martínez and M. Gutierrez-Rodríguez provided funding and revisions. M.L. Vera-Pedrosa, P. Sánchez Pérez, J.M. Ruiz Robles, S. Arias-Santiago, I. Martínez-Carrascoso, F.J. Bermúdez-Jiménez, A. Braza-Boils, and J.A. Bernal provided technical support, discussions, and revisions. F.M. Cruz and J. Jalife cowrote the article and conceived the study. J. Jalife provided supervision, funding, and revisions.

Sources of Funding

This work was supported by the National heart, Lung and Blood Institute under National Institutes of Health (NIH) grant R01HL163943; the La Caixa Banking Foundation project code HR18-00304 (grant LCF/PR/HR19/52160013); grants PI-FIS-2020, PI20/01220, PI-FIS-2023, and PI23/01039 from the Instituto de Salud Carlos III and cofunded by the Fondo Europeo de Desarrollo Regional (FEDER) and the European Union, respectively; grants PID2020-116935RB-I00 and BFU2016-75144-R funded by MICIU/AEI/10.13039/501100011033; the Fundación La Marató de TV3 (736/C/2020) amb el suport de la Fundació La Marató de TV3; the CIBER (Centro de Investigación Biomédica en Red) de Enfermedades Cardiovasculares (grant CB16/11/00458); the European Union's Horizon 2020 grant agreement GA-965286; and the Program S2022/BMD7229-CM ARCADIA-CM funded by the Comunidad de Madrid to J. Jalife; grant PID2021-126423OB-C22 (to M. Martín-Martínez) funded by MICIU/AEI/10.13039/501100011033; and European Regional Development Fund (ERDF) grant PID2022-137214OB-C22 (to M. Gutierrez-Rodríguez) funded by MICIU/AEI/10.13039/501100011033. The imaging studies were performed in the TRIMA@CNIC (Infraestructura de Imagen Traslacional Avanzada del CNIC) node of the ICTS ReDIB (Infraestructuras Científicas y Técnicas Singulares: Red Distribuida de Imagen Biomédica) grant ICTS-2018-04-CNIC-16 funded by MICIU/AEI/10.13039/501100011033 and ERDF, and project EQC2018-005070-P funded by MICIU/AEI/10.13039/501100011033 and FEDER. A.I. Moreno-Manuel holds an formación profesional universitaria (FPU) contract (FPU20/01569) from the Ministerio de Universidades. J.M. Ruiz Robles holds an FPU contract (FPU22/03253) from the Ministerio de Universidades. L.K. Gutiérrez holds an FPI contract (PRE2018-083530) from the Ministerio de Economía y Competitividad de España cofunded by the Fondo Social Europeo, attached to project SEV-2015-0505-18-2. I. Martínez-Carrascoso holds a PFIS (Contratos predoctorales de formación en investigación en salud) contract (FI21/00243) funded by Instituto de Salud Carlos III and the Fondo Social Europeo Plus cofunded by the European Union. M.L. Vera-Pedrosa held contract PEJD-2019-PRE/BMD-15982 funded by the Consejería de Educación e Investigación de la Comunidad de Madrid y Fondo Social Europeo.

Disclosures

None.

Supplemental Material

Extended Materials & Methods
Figures S1–S14
Tables S1–S5
Statistical Analyses Data
Major Resources Table
References 24,59–92

REFERENCES

1. Tawil R, Ptacek LJ, Pavlakis SG, DeVivo DC, Penn AS, Ozdemir C, Griggs RC. Andersen's syndrome: potassium-sensitive periodic paralysis, ventricular ectopy, and dysmorphic features. *Ann Neurol.* 1994;35:326–330. doi: 10.1002/ana.410350313
2. Tristani-Firouzi M, Jensen JL, Donaldson MR, Sansone V, Meola G, Hahn A, Bendahhou S, Kwiecinski H, Fidzianska A, Plaster N, et al. Functional and clinical characterization of KCNJ2 mutations associated with LQT7 (Andersen syndrome). *J Clin Invest.* 2002;110:381–388. doi: 10.1172/JCI15183
3. Plaster NM, Tawil R, Tristani-Firouzi M, Canun S, Bendahhou S, Tsunoda A, Donaldson MR, Iannaccone ST, Brunt E, Barohn R, et al. Mutations in Kir2.1 cause the developmental and episodic electrical phenotypes of Andersen's syndrome. *Cell.* 2001;105:511–519. doi: 10.1016/s0092-8674(01)00342-7
4. Yoon G, Oberoi S, Tristani-Firouzi M, Etheridge SP, Quitania L, Kramer JH, Miller BL, Fu YH, Ptacek LJ. Andersen-Tawil syndrome: prospective cohort analysis and expansion of the phenotype. *Am J Med Genet A.* 2006;140:312–321. doi: 10.1002/ajmg.a.31092
5. Manuel AIM, Gutierrez LK, Pedrosa MLV, Urendez FMC, Jimenez FJB, Carrascoso IM, Perez PS, Macias A, Jalife J. Molecular stratification of arrhythmogenic mechanisms in the Andersen Tawil Syndrome. *Cardiovasc Res.* 2022;119:919–932. doi: 10.1093/cvr/cvac118
6. Panama BK, McLerie M, Lopatin AN. Heterogeneity of IK1 in the mouse heart. *Am J Physiol Heart Circ Physiol.* 2007;293:H3558–H3567. doi: 10.1152/ajpheart.00419.2007
7. Dhamoon AS, Jalife J. The inward rectifier current (IK1) controls cardiac excitability and is involved in arrhythmogenesis. *Heart Rhythm.* 2005;2:316–324. doi: 10.1016/j.hrthm.2004.11.012
8. Pegan S, Arrabit C, Slesinger PA, Choe S. Andersen's syndrome mutation effects on the structure and assembly of the cytoplasmic domains of Kir2.1. *Biochemistry.* 2006;45:8599–8606. doi: 10.1021/bi060653d
9. Handklo-Jamal R, Meisel E, Yakubovich D, Vysochek L, Beinart R, Glikson M, McMullen JR, Dascal N, Nof E, Oz S. Andersen-Tawil syndrome is associated with impaired PIP2 regulation of the potassium channel Kir2.1. *Front Pharmacol.* 2020;11:672. doi: 10.3389/fphar.2020.00672

10. Lopes CM, Zhang H, Rohacs T, Jin T, Yang J, Logothetis DE. Alterations in conserved Kir channel-PIP2 interactions underlie channelopathies. *Neuron*. 2002;34:933–944. doi: 10.1016/s0896-6273(02)00725-0
11. Donaldson MR, Jensen JL, Tristani-Firouzi M, Tawil R, Bendahhou S, Suarez WA, Cobo AM, Poza JJ, Behr E, Wagstaff J, et al. PIP2 binding residues of Kir2.1 are common targets of mutations causing Andersen syndrome. *Neurology*. 2003;60:1811–1816. doi: 10.1212/01.wnl.0000072261.14060.47
12. Cho HC, Tsushima RG, Nguyen TT, Guy HR, Backx PH. Two critical cysteine residues implicated in disulfide bond formation and proper folding of Kir2.1. *Biochemistry*. 2000;39:4649–4657. doi: 10.1021/bi992469g
13. Marino SM, Gladyshev VN. Analysis and functional prediction of reactive cysteine residues. *J Biol Chem*. 2012;287:4419–4425. doi: 10.1074/jbc.R111.275578
14. Garneau L, Klein H, Parent L, Sauve R. Contribution of cytosolic cysteine residues to the gating properties of the Kir2.1 inward rectifier. *Biophys J*. 2003;84:3717–3729. doi: 10.1016/S0006-3495(03)75100-5
15. Gomez R, Caballero R, Barana A, Amoros I, De Palm SH, Matamoros M, Nunez M, Perez-Hernandez M, Iriepa I, Tamargo J, et al. Structural basis of drugs that increase cardiac inward rectifier Kir2.1 currents. *Cardiovasc Res*. 2014;104:337–346. doi: 10.1093/cvr/cvu203
16. Caballero R, Dolz-Gaiton P, Gomez R, Amoros I, Barana A, Gonzalez de la Fuente M, Osuna L, Duarte J, Lopez-Izquierdo A, Moraleda I, et al. Flecainide increases Kir2.1 currents by interacting with cysteine 311, decreasing the polyamine-induced rectification. *Proc Natl Acad Sci USA*. 2010;107:15631–15636. doi: 10.1073/pnas.1004021107
17. Bannister JP, Young BA, Sivaprasadarao A, Wray D. Conserved extracellular cysteine residues in the inwardly rectifying potassium channel Kir2.3 are required for function but not expression in the membrane. *FEBS Lett*. 1999;458:393–399. doi: 10.1016/s0014-5793(99)01096-0
18. Leyland ML, Dart C, Spencer PJ, Sutcliffe MJ, Stanfield PR. The possible role of a disulphide bond in forming functional Kir2.1 potassium channels. *Pflugers Arch*. 1999;438:778–781. doi: 10.1007/s004249900153
19. Fernandes CAH, Zuniga D, Fagnen C, Kugler V, Scala R, Pehau-Arnaudet G, Wagner R, Perahia D, Bendahhou S, Venien-Bryan C. Cryo-electron microscopy unveils unique structural features of the human Kir2.1 channel. *Sci Adv*. 2022;8:eabq8489. doi: 10.1126/sciadv.abq8489
20. Xiao X, Li J, Samulski RJ. Production of high-titer recombinant adeno-associated virus vectors in the absence of helper adenovirus. *J Virol*. 1998;72:2224–2232. doi: 10.1128/JVI.72.3.2224-2232.1998
21. Hauswirth WW, Lewin AS, Zolotukhin S, Muzyczka N. Production and purification of recombinant adeno-associated virus. *Methods Enzymol*. 2000;316:743–761. doi: 10.1016/s0076-6879(00)16760-6
22. Cruz FM, Sanz-Rosa D, Roche-Molina M, Garcia-Prieto J, Garcia-Ruiz JM, Pizarro G, Jimenez-Borreguero LJ, Torres M, Bernad A, Ruiz-Cabello J, et al. Exercise triggers ARVC phenotype in mice expressing a disease-causing mutated version of human plakophilin-2. *J Am Coll Cardiol*. 2015;65:1438–1450. doi: 10.1016/j.jacc.2015.01.045
23. Bao Y, Willis BC, Frasier CR, Lopez-Santiago LF, Lin X, Ramos-Mondragon R, Auerbach DS, Chen C, Wang Z, Anumonwo J, et al. Scn2b deletion in mice results in ventricular and atrial arrhythmias. *Circ Arrhythm Electrophysiol*. 2016;9:e003923. doi: 10.1161/CIRCEP.116.003923
24. Macías A, González-Guerra A, Moreno-Manuel AI, Cruz FM, Gutiérrez LK, García-Quintáns N, Roche-Molina M, Bermúdez-Jiménez F, Andrés V, Vera-Pedrosa ML, et al. Kir2.1 dysfunction at the sarcolemma and the sarcoplasmic reticulum causes arrhythmias in a mouse model of Andersen–Tawil syndrome type 1. *Nat Cardiovasc Res*. 2022;1:900–917. doi: 10.1038/s44161-022-00145-2
25. Cabanos C, Wang M, Han X, Hansen SB. A soluble fluorescent binding assay reveals PIP2 antagonism of TREK-1 channels. *Cell Rep*. 2017;20:1287–1294. doi: 10.1016/j.celrep.2017.07.034
26. Semenov I, Grigoryev S, Neuber JU, Zemlin CW, Pakhomova ON, Casciola M, Pakhomov AG. Excitation and injury of adult ventricular cardiomyocytes by nano- to millisecond electric shocks. *Sci Rep*. 2018;8:8233. doi: 10.1038/s41598-018-26521-2
27. Brette F, Despa S, Bers DM, Orchard CH. Spatiotemporal characteristics of SR Ca(2+) uptake and release in detubulated rat ventricular myocytes. *J Mol Cell Cardiol*. 2005;39:804–812. doi: 10.1016/j.yjmcc.2005.08.005
28. Macias A, Diaz-Larrosa JJ, Blanco Y, Fanjul V, Gonzalez-Gomez C, Gonzalo P, Andres-Manzano MJ, da Rocha AM, Ponce-Balbuena D, Allan A, et al. Paclitaxel mitigates structural alterations and cardiac conduction system defects in a mouse model of Hutchinson-Gilford progeria syndrome. *Cardiovasc Res*. 2021;118:503–516. doi: 10.1093/cvr/cvab055
29. Symanzik J. Statistical analysis of spatial point patterns. *Technometrics*. 2005;47:516–517. doi: 10.1198/tech.2005.s318
30. Yu G, Chakrabarti S, Tischenko M, Chen AL, Wang Z, Cho H, French BA, Naga Prasad SV, Chen Q, Wang QK. Gene therapy targeting protein trafficking regulator MOG1 in mouse models of Brugada syndrome, arrhythmias, and mild cardiomyopathy. *Sci Transl Med*. 2022;14:eabf3136. doi: 10.1126/scitranslmed.abf3136
31. Bezzerides VJ, Caballero A, Wang S, Ai Y, Hylind RJ, Lu F, Heims-Waldron DA, Chambers KD, Zhang D, Abrams DJ, et al. Gene therapy for catecholaminergic polymorphic ventricular tachycardia by inhibition of Ca(2+)/calmodulin-dependent kinase II. *Circulation*. 2019;140:405–419. doi: 10.1161/CIRCULATIONAHA.118.038514
32. Schram G, Melnyk P, Pourrier M, Wang Z, Nattel S. Kir2.4 and Kir2.1 K(+) channel subunits co-assemble: a potential new contributor to inward rectifier current heterogeneity. *J Physiol*. 2002;544:337–349. doi: 10.1113/jphysiol.2002.026047
33. Ballester LY, Benson DW, Wong B, Law IH, Mathews KD, Vanoye CG, George AL Jr. Trafficking-competent and trafficking-defective KCNJ2 mutations in Andersen syndrome. *Hum Mutat*. 2006;27:388. doi: 10.1002/humu.9418
34. Haruna Y, Kobori A, Makiyama T, Yoshida H, Akao M, Doi T, Tsuji K, Ono S, Nishio Y, Shimizu W, et al. Genotype-phenotype correlations of KCNJ2 mutations in Japanese patients with Andersen-Tawil syndrome. *Hum Mutat*. 2007;28:208. doi: 10.1002/humu.9483
35. Ma D, Taneja TK, Hagen BM, Kim BY, Ortega B, Lederer WJ, Welling PA. Golgi export of the Kir2.1 channel is driven by a trafficking signal located within its tertiary structure. *Cell*. 2011;145:1102–1115. doi: 10.1016/j.cell.2011.06.007
36. Perez-Hernandez M, Matamoros M, Alfayate S, Nieto-Marin P, Utrilla RG, Tinaquero D, de Andres R, Crespo T, Ponce-Balbuena D, Willis BC, et al. Brugada syndrome trafficking-defective Nav1.5 channels can trap cardiac Kir2.1/2.2 channels. *JCI Insight*. 2018;3:e96291. doi: 10.1172/jci.insight.96291
37. Pini J, Giuliano S, Matonti J, Gannoun L, Simkin D, Rouleau M, Bendahhou S. Osteogenic and chondrogenic master genes expression is dependent on the Kir2.1 potassium channel through the bone morphogenetic protein pathway. *J Bone Miner Res*. 2018;33:1826–1841. doi: 10.1002/jbmr.3474
38. Hansen SB, Tao X, MacKinnon R. Structural basis of PIP2 activation of the classical inward rectifier K+ channel Kir2.2. *Nature*. 2011;477:495–498. doi: 10.1038/nature10370
39. Lee SJ, Ren F, Zangerl-Plessl EM, Heyman S, Stary-Weinzinger A, Yuan P, Nichols CG. Structural basis of control of inward rectifier Kir2 channel gating by bulk anionic phospholipids. *J Gen Physiol*. 2016;148:227–237. doi: 10.1085/jgp.201611616
40. Zangerl-Plessl EM, Lee SJ, Maksaev G, Bernsteiner H, Ren F, Yuan P, Stary-Weinzinger A, Nichols CG. Atomistic basis of opening and conduction in mammalian inward rectifier potassium (Kir2.2) channels. *J Gen Physiol*. 2020;152:e201912422. doi: 10.1085/jgp.201912422
41. Fagnen C, Bannwarth L, Oubella I, Forest E, De Zorzi R, de Araujo A, Mhoumadi Y, Bendahhou S, Perahia D, Venien-Bryan C. New Structural insights into Kir channel gating from molecular simulations, HDX-MS and functional studies. *Sci Rep*. 2020;10:8392. doi: 10.1038/s41598-020-65246-z
42. Gadsby DC, Cranefield PF. Two levels of resting potential in cardiac Purkinje fibers. *J Gen Physiol*. 1977;70:725–746. doi: 10.1085/jgp.70.6.725
43. Suh BC, Hille B. PIP2 is a necessary cofactor for ion channel function: how and why? *Annu Rev Biophys*. 2008;37:175–195. doi: 10.1146/annurev.biophys.37.032807.125859
44. Tully I, Atherton J, Hunt L, Ingles J, Semsarian C, McGaughran J. Rarity and phenotypic heterogeneity provide challenges in the diagnosis of Andersen-Tawil syndrome: two cases presenting with ECGs mimicking catecholaminergic polymorphic ventricular tachycardia (CPVT). *Int J Cardiol*. 2015;201:473–475. doi: 10.1016/j.ijcard.2015.07.069
45. Kukla P, Biernacka EK, Baranchuk A, Jastrzebski M, Jagodzinska M. Electrocardiogram in Andersen-Tawil syndrome. New electrocardiographic criteria for diagnosis of type-1 Andersen-Tawil syndrome. *Curr Cardiol Rev*. 2014;10:222–228. doi: 10.2174/1573403x10666140514102528
46. Bannister ML, MacLeod KT, George CH. Moving in the right direction: elucidating the mechanisms of interaction between flecainide and the cardiac ryanodine receptor. *Br J Pharmacol*. 2022;179:2558–2563. doi: 10.1111/bph.15718
47. Soom M, Schonherr R, Kubo Y, Kirsch C, Klinger R, Heinemann SH. Multiple PIP2 binding sites in Kir2.1 inwardly rectifying potassium channels. *FEBS Lett*. 2001;490:49–53. doi: 10.1016/s0014-5793(01)02136-6
48. Zsolnay V, Fill M, Gillespie D. Sarcoplasmic reticulum Ca(2+) release uses a cascading network of intra-SR and channel countercurrents. *Biophys J*. 2018;114:462–473. doi: 10.1016/j.bpj.2017.11.3775
49. Katan M, Cockcroft S. Phosphatidylinositol(4,5)bisphosphate: diverse functions at the plasma membrane. *Essays Biochem*. 2020;64:513–531. doi: 10.1042/EBC20200041
50. Abriel H, Rougier JS, Jalife J. Ion channel macromolecular complexes in cardiomyocytes: roles in sudden cardiac death. *Circ Res*. 2015;116:1971–1988. doi: 10.1161/CIRCRESAHA.116.305017

51. Meadows LS, Isom LL. Sodium channels as macromolecular complexes: implications for inherited arrhythmia syndromes. *Cardiovasc Res*. 2005;67:448–458. doi: 10.1016/j.cardiores.2005.04.003
52. Willis BC, Ponce-Balbuena D, Jalife J. Protein assemblies of sodium and inward rectifier potassium channels control cardiac excitability and arrhythmogenesis. *Am J Physiol Heart Circ Physiol*. 2015;308:H1463–H1473. doi: 10.1152/ajpheart.00176.2015
53. Siegel MR, Sisler HD. Inhibition of protein synthesis in vitro by cycloheximide. *Nature*. 1963;200:675–676. doi: 10.1038/200675a0
54. Milstein ML, Musa H, Balbuena DP, Anumonwo JM, Auerbach DS, Furspan PB, Hou L, Hu B, Schumacher SM, Vaidyanathan R, et al. Dynamic reciprocity of sodium and potassium channel expression in a macromolecular complex controls cardiac excitability and arrhythmia. *Proc Natl Acad Sci USA*. 2012;109:E2134–E2143. doi: 10.1073/pnas.1109370109
55. Gavillet B, Rougier JS, Domenighetti AA, Behar R, Boixel C, Ruchat P, Lehr HA, Pedrazzini T, Abriel H. Cardiac sodium channel Nav1.5 is regulated by a multiprotein complex composed of syntrophins and dystrophin. *Circ Res*. 2006;99:407–414. doi: 10.1161/01.RES.0000237466.13252.5e
56. Petitprez S, Zmoos AF, Ogrodnik J, Balse E, Raad N, El-Haou S, Albesa M, Bittihn P, Luther S, Lehnart SE, et al. SAP97 and dystrophin macromolecular complexes determine two pools of cardiac sodium channels Nav1.5 in cardiomyocytes. *Circ Res*. 2011;108:294–304. doi: 10.1161/CIRCRESAHA.110.228312
57. Leonoudakis D, Mailliard W, Wingerd K, Clegg D, Vandenberg C. Inward rectifier potassium channel Kir2.2 is associated with synapse-associated protein SAP97. *J Cell Sci*. 2001;114:987–998. doi: 10.1242/jcs.114.5.987
58. Gada KD, Kamuene JM, Chandrashekar A, Kissell RC, Yauch AK, Plant LD. PI(4,5)P2 regulates the gating of NaV1.4 channels. *J Gen Physiol*. 2023;155:e202213255. doi: 10.1085/jgp.202213255
59. Ponce-Balbuena D, Guerrero-Serna G, Valdivia CR, Caballero R, Diez-Guerra FJ, Jimenez-Vazquez EN, Ramirez RJ, Monteiro da Rocha A, Herron TJ, Campbell KF, et al. Cardiac Kir2.1 and NaV1.5 channels traffic together to the sarcolemma to control excitability. *Circ Res*. 2018;122:1501–1516. doi: 10.1161/CIRCRESAHA.117.311872
60. Mitchell GF, Jeron A, Koren G. Measurement of heart rate and Q-T interval in the conscious mouse. *Am J Physiol*. 1998;274:H747–H751. doi: 10.1152/ajpheart.1998.274.3.H747
61. Moreno C, Prieto P, Macias A, Pimentel-Santillana M, de la Cruz A, Traves PG, Bosca L, Valenzuela C. Modulation of voltage-dependent and inward rectifier potassium channels by 15-epi-lipoxin-A4 in activated murine macrophages: implications in innate immunity. *J Immunol*. 2013;191:6136–6146. doi: 10.4049/jimmunol.1300235
62. Cerrone M, Noujaim SF, Tolkacheva EG, Talkachou A, O'Connell R, Berenfeld O, Anumonwo J, Pandit SV, Vikstrom K, Napolitano C, et al. Arrhythmogenic mechanisms in a mouse model of catecholaminergic polymorphic ventricular tachycardia. *Circ Res*. 2007;101:1039–1048. doi: 10.1161/CIRCRESAHA.107.148064
63. Fernandez MC, Kopton RA, Simon-Chica A, Madl J, Hilgendorf I, Zgierski-Johnston CM, Schneider-Warme F. Channelrhodopsins for cell-type specific illumination of cardiac electrophysiology. *Methods Mol Biol*. 2021;2191:287–307. doi: 10.1007/978-1-0716-0830-2_17
64. Andre I, Bradley P, Wang C, Baker D. Prediction of the structure of symmetrical protein assemblies. *Proc Natl Acad Sci USA*. 2007;104:17656–17661. doi: 10.1073/pnas.0702626104
65. Khatib F, Cooper S, Tyka MD, Xu K, Makedon I, Popovic Z, Baker D, Players F. Algorithm discovery by protein folding game players. *Proc Natl Acad Sci USA*. 2011;108:18949–18953. doi: 10.1073/pnas.1115898108
66. Fleishman SJ, Leaver-Fay A, Corn JE, Strauch EM, Khare SD, Koga N, Ashworth J, Murphy P, Richter F, Lemmon G, et al. RosettaScripts: a scripting language interface to the Rosetta macromolecular modeling suite. *PLoS One*. 2011;6:e20161. doi: 10.1371/journal.pone.0020161
67. DiMaio F, Leaver-Fay A, Bradley P, Baker D, Andre I. Modeling symmetric macromolecular structures in Rosetta3. *PLoS One*. 2011;6:e20450. doi: 10.1371/journal.pone.0020450
68. Lomize MA, Pogozheva ID, Joo H, Mosberg HI, Lomize AL. OPM database and PPM web server: resources for positioning of proteins in membranes. *Nucleic Acids Res*. 2012;40:D370–D376. doi: 10.1093/nar/gkr703
69. Dong R, Pan S, Peng Z, Zhang Y, Yang J. mTM-align: a server for fast protein structure database search and multiple protein structure alignment. *Nucleic Acids Res*. 2018;46:W380–W386. doi: 10.1093/nar/gky430
70. Dong R, Peng Z, Zhang Y, Yang J.mTM-align: an algorithm for fast and accurate multiple protein structure alignment. *Bioinformatics*. 2018;34:1719–1725. doi: 10.1093/bioinformatics/btx828
71. Baker NA, Sept D, Joseph S, Holst MJ, McCammon JA. Electrostatics of nanosystems: application to microtubules and the ribosome. *Proc Natl Acad Sci USA*. 2001;98:10037–10041. doi: 10.1073/pnas.181342398
72. Dolinsky TJ, Nielsen JE, McCammon JA, Baker NA. PDB2PQR: an automated pipeline for the setup of Poisson-Boltzmann electrostatics calculations. *Nucleic Acids Res*. 2004;32:W665–W667. doi: 10.1093/nar/gkh381
73. Alford RF, Koehler Leman J, Weitzner BD, Duran AM, Tilley DC, Elazar A, Gray JJ. An integrated framework advancing membrane protein modeling and design. *PLoS Comput Biol*. 2015;11:e1004398. doi: 10.1371/journal.pcbi.1004398
74. Capra JA, Laskowski RA, Thornton JM, Singh M, Funkhouser TA. Predicting protein ligand binding sites by combining evolutionary sequence conservation and 3D structure. *PLoS Comput Biol*. 2009;5:e1000585. doi: 10.1371/journal.pcbi.1000585
75. Pravda L, Sehnal D, Tousek D, Navratilova V, Bazgier V, Berka K, Svobodova Varekova R, Koca J, Otyepka M. MOLEonline: a web-based tool for analyzing channels, tunnels and pores (2018 update). *Nucleic Acids Res*. 2018;46:W368–W373. doi: 10.1093/nar/gky309
76. Jacobson MP, Friesner RA, Xiang Z, Honig B. On the role of the crystal environment in determining protein side-chain conformations. *J Mol Biol*. 2002;320:597–608. doi: 10.1016/s0022-2836(02)00470-9
77. Jacobson MP, Pincus DL, Rapp CS, Day TJ, Honig B, Shaw DE, Friesner RA. A hierarchical approach to all-atom protein loop prediction. *Proteins*. 2004;55:351–367. doi: 10.1002/prot.10613
78. Laskowski RA, MacArthur MW, Moss DS, Thornton JM. PROCHECK: a program to check the stereochemical quality of protein structures. *J Appl Crystallogr*. 1993;26:283–291. doi: 10.1107/s0021889892009944
79. Sastry GM, Adzhigirey M, Day T, Annabhimoju R, Sherman W. Protein and ligand preparation: parameters, protocols, and influence on virtual screening enrichments. *J Comput Aided Mol Des*. 2013;27:221–234. doi: 10.1007/s10822-013-9644-8
80. Jo S, Kim T, Im W. Automated builder and database of protein/membrane complexes for molecular dynamics simulations. *PLoS One*. 2007;2:e880. doi: 10.1371/journal.pone.0000880
81. Jo S, Kim T, Iyer VG, Im W. CHARMM-GUI: a web-based graphical user interface for CHARMM. *J Comput Chem*. 2008;29:1859–1865. doi: 10.1002/jcc.20945
82. Jo S, Lim JB, Klauda JB, Im W. CHARMM-GUI Membrane Builder for mixed bilayers and its application to yeast membranes. *Biophys J*. 2009;97:50–58. doi: 10.1016/j.bpj.2009.04.013
83. Wu EL, Cheng X, Jo S, Rui H, Song KC, Davila-Contreras EM, Qi Y, Lee J, Monje-Galvan V, Venable RM, et al. CHARMM-GUI Membrane Builder toward realistic biological membrane simulations. *J Comput Chem*. 2014;35:1997–2004. doi: 10.1002/jcc.23702
84. Lee J, Hitzenberger M, Rieger M, Kern NR, Zacharias M, Im W. CHARMM-GUI supports the Amber force fields. *J Chem Phys*. 2020;153:035103. doi: 10.1063/5.0012280
85. Lomize AL, Pogozheva ID, Lomize MA, Mosberg HI. Positioning of proteins in membranes: a computational approach. *Protein Sci*. 2006;15:1318–1333. doi: 10.1110/ps.062126106
86. Lomize AL, Pogozheva ID, Mosberg HI. Anisotropic solvent model of the lipid bilayer. 2. Energetics of insertion of small molecules, peptides, and proteins in membranes. *J Chem Inf Model*. 2011;51:930–946. doi: 10.1021/ci200020k
87. Jorgensen WL, Chandrasekhar J, Madura JD, Impey RW, Klein ML. Comparison of simple potential functions for simulating liquid water. *J Chem Phys*. 1983;79:926–935. doi: 10.1063/1.445869
88. Tian C, Kasavajhala K, Belfon KAA, Raguette L, Huang H, Migues AN, Bickel J, Wang Y, Pincay J, Wu Q, et al. ff19SB: Amino-Acid-Specific protein backbone parameters trained against quantum mechanics energy surfaces in solution. *J Chem Theory Comput*. 2020;16:528–552. doi: 10.1021/acs.jctc.9b00591
89. Case DA, Aktulga HM, Belfon K, Cerutti DS, Cisneros GA, Cruzeiro VWD, Forouzesh N, Giese TJ, Götz AW, Gohlke H, et al. AmberTools. *J Chem Inf Model*. 2023;63:6183–6191. doi: 10.1021/acs.jcim.3c01153
90. Sweet CR, Petrone P, Pande VS, Izaguirre JA. Normal mode partitioning of Langevin dynamics for biomolecules. *J Chem Phys*. 2008;128:145101. doi: 10.1063/1.2883966
91. Berendsen HJC, Postma JPM, Gunsteren WF, DiNola A, Haak JR. Molecular dynamics with coupling to an external bath. *J Chem Phys*. 1984;81:3684–3690. doi: 10.1063/1.448118
92. Roe DR, Cheatham TE, 3rd. PTRAJ and CPPTRAJ: software for processing and analysis of molecular dynamics trajectory data. *J Chem Theory Comput*. 2013;9:3084–3095. doi: 10.1021/ct400341p